Radiative impacts of Californian marine low clouds on North Pacific climate

Ayumu Miyamoto[1], Hisashi Nakamura[2,3], Shang-Ping Xie[1], Takafumi Miyasaka[2], and Yu Kosaka[2]

[1]Scripps Institution of Oceanography, University of California San Diego
[2]Research Center for Advanced Science and Technology, The University of Tokyo
[3]Japan Agency for Marine-Earth Science and Technology

August 8, 2023

Abstract

The northeastern Pacific climate system is featured by an extensive low-cloud deck off California on the southeastern flank of the subtropical high that accompanies intense northeasterly trades and relatively low sea surface temperatures (SSTs). This study assesses climatological impacts of the low-cloud deck and their seasonal differences by regionally turning on and off the low-cloud radiative effect in a fully coupled atmosphere-ocean model. The simulations demonstrate that the cloud radiative effect causes a local SST decrease of up to 3°C on an annual average with the response extending southwestward with intensified trade winds, indicative of the wind-evaporation-SST (WES) feedback. This non-local wind response is strong in summer, when the SST decrease peaks due to increased shortwave cooling, and persists into autumn. In these seasons when the background SST is high, the lowered SST suppresses deep-convective precipitation that would otherwise occur in the absence of the low-cloud deck. The resultant anomalous diabatic cooling induces a surface anticyclonic response with the intensified trades that promote the WES feedback. Such seasonal enhancement of the atmospheric response does not occur without air-sea couplings. The enhanced trades accompany intensified upper-tropospheric westerlies, strengthening the vertical wind shear that, together with the lowered SST, acts to shield Hawaii from powerful hurricanes. On the basin scale, the anticyclonic surface wind response accelerates the North Pacific subtropical ocean gyre to speed up the Kuroshio by as much as 30%. SST thereby increases along the Kuroshio and its extension, intensifying upward turbulent heat fluxes from the ocean to increase precipitation.

Radiative impacts of Californian marine low clouds on North Pacific climate

Ayumu Miyamoto,[a] Hisashi Nakamura,[b,c] Shang-Ping Xie,[a] Takafumi Miyasaka,[b] and Yu Kosaka,[b]

[a] *Scripps Institution of Oceanography, University of California San Diego, La Jolla, California, USA* [b] *Research Center for Advanced Science and Technology, The University of Tokyo, Tokyo, Japan*

[c] *Japan Agency for Marine-Earth Science and Technology, Yokohama, Japan*

Revised manuscript submitted to Journal of Climate on August 5th, 2023

Corresponding author: Ayumu Miyamoto, aymiyamoto@ucsd.edu

ABSTRACT: The northeastern Pacific climate system is featured by an extensive low-cloud deck off California on the southeastern flank of the subtropical high that accompanies intense northeasterly trades and relatively low sea surface temperatures (SSTs). This study assesses climatological impacts of the low-cloud deck and their seasonal differences by regionally turning on and off the low-cloud radiative effect in a fully coupled atmosphere-ocean model. The simulations demonstrate that the cloud radiative effect causes a local SST decrease of up to 3°C on an annual average with the response extending southwestward with intensified trade winds, indicative of the wind-evaporation-SST (WES) feedback. This non-local wind response is strong in summer, when the SST decrease peaks due to increased shortwave cooling, and persists into autumn. In these seasons when the background SST is high, the lowered SST suppresses deep-convective precipitation that would otherwise occur in the absence of the low-cloud deck. The resultant anomalous diabatic cooling induces a surface anticyclonic response with the intensified trades that promote the WES feedback. Such seasonal enhancement of the atmospheric response does not occur without air-sea couplings. The enhanced trades accompany intensified upper-tropospheric westerlies, strengthening the vertical wind shear that, together with the lowered SST, acts to shield Hawaii from powerful hurricanes. On the basin scale, the anticyclonic surface wind response accelerates the North Pacific subtropical ocean gyre to speed up the Kuroshio by as much as 30%. SST thereby increases along the Kuroshio and its extension, intensifying upward turbulent heat fluxes from the ocean to increase precipitation.

1. Introduction

Over each of the subtropical oceans, large-scale surface winds are characterized by subtropical highs (e.g., Rodwell and Hoskins 2001; Seager et al. 2003; Miyasaka and Nakamura 2005, 2010; Nakamura et al. 2010; Miyamoto et al. 2022b). To the east of a subtropical high, enhanced lower-tropospheric stability due to mid-tropospheric subsidence and low sea surface temperature (SST) promotes abundant low clouds (e.g., Klein and Hartmann 1993; Wood and Bretherton 2006; Miyamoto et al. 2018). Since low clouds reflect a substantial fraction of incoming shortwave radiation, they are crucial in Earth's energy budget (Hartmann et al. 1992) and its perturbations such as global warming (Bony et al. 2005; Zelinka et al. 2020).

The cooling effect of low clouds is also important in regional climate through air-sea interactions. Reflecting insolation, low clouds act to reinforce the underlying low SST. This results in stronger lower-tropospheric stability, which facilitates low-cloud formation. This local feedback, known as positive low cloud-SST feedback, has been identified as crucial air-sea coupled feedback over the eastern subtropical oceans (e.g., Norris and Leovy 1994; Clement et al. 2009; Myers et al. 2018; Middlemas et al. 2019; Yang et al. 2023).

In addition to the local impacts on SST, low clouds have been suggested to have non-local effects. As low SST over the eastern subtropical oceans is important in maintaining the subtropical high (Seager et al. 2003; Miyasaka and Nakamura 2005, 2010), SST cooling by low clouds is suggested to reinforce the subtropical high. They can also reinforce the subtropical high through cloud-top longwave cooling (Miyasaka and Nakamura 2005, 2010). Strengthened trade winds associated with the enhanced subtropical high act to lower SST by promoting evaporation from the ocean. This wind-evaporation-SST (WES) feedback (Xie and Philander 1994) propagates westward, yielding remote influence on the equatorial oceans (Xie et al. 2007; Bellomo et al. 2014; Yang et al. 2023). Nevertheless, it has been controversial to what extent it is actually effective in climatology (Seager et al. 2003; Miyasaka and Nakamura 2005, 2010; Kawai and Koshiro et al. 2020). One reason for this is the difficulty in evaluating the influence of low clouds in the air-sea coupled system. Here, we evaluate the low-cloud feedback using an atmosphere-ocean general circulation model (AOGCM).

Recently, Miyamoto et al. (2021, 2022a) regionally disabled low-cloud radiative effects (CRE) in a fully coupled AOGCM. Specifically, low clouds were made transparent regionally to evaluate specific low-cloud impacts in a fully coupled system. This technique was employed in the Clouds On-Off Klimate Model Intercomparison Experiment using atmosphere-only models (COOKIE; Stevens et al. 2012; Voigt et al. 2021), but we applied it to an AOGCM. Such coupled simulations conducted for the South Indian Ocean demonstrated that low-cloud feedback is essential in the formation of the summertime subtropical Mascarene high (Miyamoto et al. 2021). Lowered SST by low clouds prevents the intertropical convergence zone (ITCZ) from expanding poleward, suppressing deep-convective precipitation on the poleward flank of the ITCZ. The resultant anomalous diabatic cooling reinforces the surface Mascarene high and promotes the WES feedback. By contrast, the low-cloud feedback is modest in winter, when the suppression of deep-convective precipitation by low clouds is less effective due to climatologically low SST (Miyamoto et al. 2022a).

The northeastern Pacific (NEP) has been recognized as a major low-cloud region (e.g., Klein and Hartmann 1993). Figure 1 shows observational climatologies of annual-mean low-cloud fraction (LCF), SST, and surface winds over the NEP. The subtropical high resides over the eastern portion of the basin, and the northeasterly trade winds blow on its southeastern flank. Over local minima of SST, LCF maximizes off the California coast. Recent modeling studies showed that, on interannual and decadal time scales, fluctuations of these low clouds act to increase SST variance locally through low cloud-SST feedback and non-locally through the WES feedback (Bellomo et al. 2014; Burgman et al. 2017; Middlemas et al. 2019; Yang et al. 2023). Applying the same methodology as in Miyamoto et al. (2021, 2022a) to the North Pacific, this study assesses the climatological impacts of low clouds over the NEP and their seasonal differences, which have not been quantified thus far. This study uses neither a slab-ocean coupled model (Bellomo et al. 2014) nor perturbs cloud radiation globally (Burgman et al. 2017; Middlemas et al. 2019; Kawai and Koshiro 2020; Yang et al. 2023) so that we can purely extract the low-cloud impacts in a fully coupled system. We examine not only the low-cloud impacts on the subtropical high and SST over the NEP but also their implications on the climate around Hawaii and the Kuroshio region.

The rest of the paper is organized as follows. Section 2 describes data and model experiments. Section 3 examines the low-cloud impacts on the subtropical high and SST over the NEP. Section 4 discusses implications on the climate in the Hawaii and Kuroshio regions. Section 5 summarizes the present study.

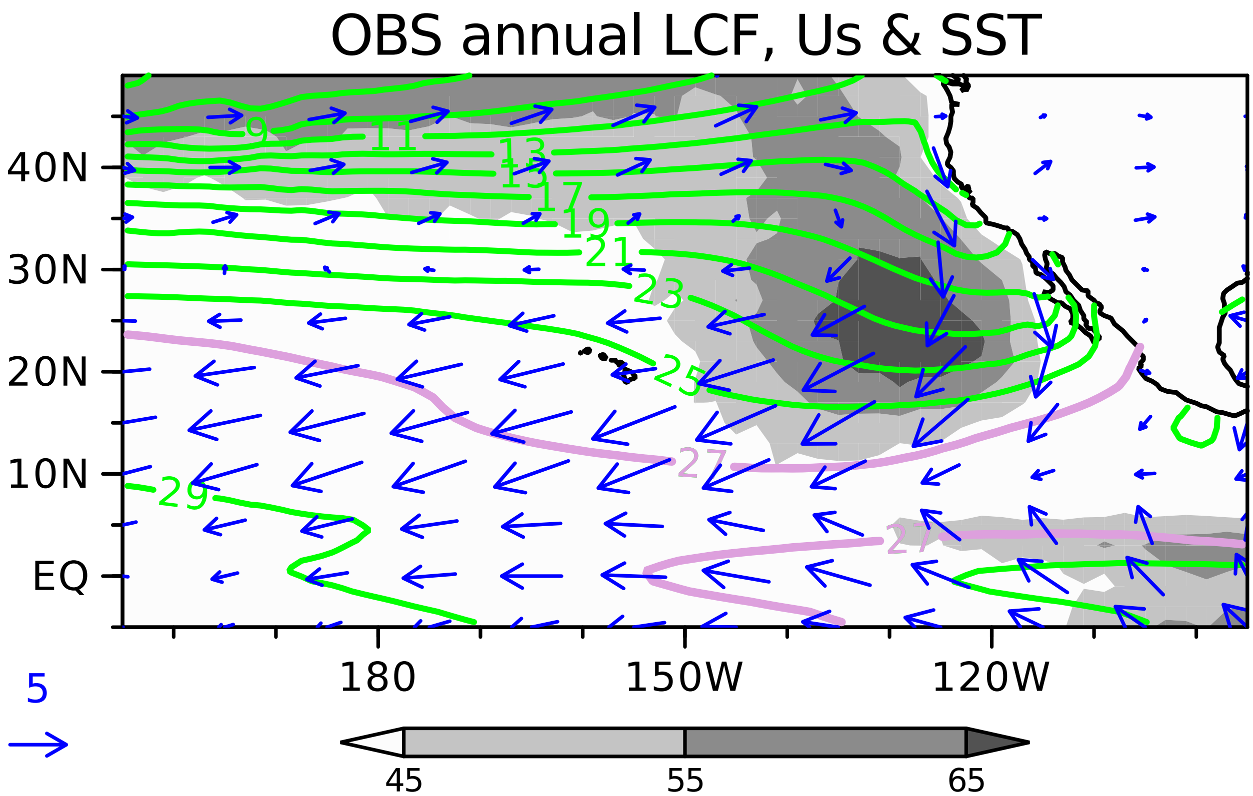

88 FIG. 1. Climatological annual-mean distributions of CALIPSO-GOCCP low-cloud fraction (%; color shaded as indicated at the bottom), OISST sea surface temperature (contoured for every 2°C in green with 27°C isotherms in purple), and JRA-55 surface winds (m s^{-1}; arrows with reference on the bottom). See Section 2 for details of the data.

2. Data and model experiments

a. Model experiments

We used the Geophysical Fluid Dynamics Laboratory (GFDL) Coupled Model version 2.1 (CM2.1; Delworth et al. 2006). Its atmospheric component has $2.5° \times 2°$ resolution in longitude-latitude with 24 vertical levels. The resolution of the 50-level ocean model is 1° in both latitude and longitude, with meridional resolution equatorward of 30° progressively finer to 1/3° at the equator. Following Miyamoto et al. (2021, 2022a), radiative impacts of low clouds are evaluated by setting maritime cloud fraction to zero over a given geographical domain for radiation calculations in CM2.1. We specify the domain [150°W-110°W, 16°N-32°N] in the subtropical NEP (black rectangles in Fig. 2; hereafter referred to as the NEP box), in which cloud fraction is set to zero artificially from the surface up to the 680-hPa level. After branched off from the same initial condition, both the low-cloud-off (CM_NoCRE) and control (CM_CTL) experiments are integrated for 110 years with the 1990-level radiative forcing. We analyze 100 years until November in the final year. A response to the low-cloud radiative effects simulated in CM2.1 is represented as CM_CTL−CM_NoCRE, which has the same sign as the low-cloud impacts. Within this analysis period, a model drift resulting from the low-cloud removal is found negligible: Radiative imbalance at the top of the atmosphere (TOA) in the last 100 years is 1.02 W m^{-2} in CM_CTL and 1.07 W m^{-2} in CM_NoCRE.

To isolate the SST influence simulated in CM2.1, we also conduct experiments with its atmospheric component (GFDL AM2.1). A control experiment (AM_CTL) is carried out with climatological SST and sea ice concentration in CM_CTL. One sensitivity experiment aimed at evaluating the NEP SST influence is AM_NEPsst, where the prescribed SST is replaced by the CM_NoCRE climatology regionally over the NEP (180°-110°W, 10°N-32°N; note a slight difference from the NEP box). AM_CTL−AM_NEPsst extracts the influence of the low-cloud induced SST anomalies over the NEP on the atmosphere (the same sign as the low-cloud impacts). Another sensitivity experiment to isolate low-cloud impacts without SST changes is AM_NoCRE_sstFixed, where radiative effects of Californian low clouds are eliminated as in CM_NoCRE but SST and sea ice are fixed to the CM_CTL climatology. AM_CTL−AM_NoCRE_sstFixed reveals the low-cloud impacts without air-sea couplings. Each of the AM2.1 experiments has been integrated for 51 years, and 50 years until the last November are analyzed. Table 1 summarizes the differences among the model experiments. The statistical significance of the model responses is determined with a Student's *t* test.

Finally, we compare the simulated climatological TOA CRE with historical simulations which participated in the Coupled Model Intercomparison Project Phase 6 (CMIP6). Only the first member run (r1i1p1) for each model is used for calculating climatology from 1980 through 2013.

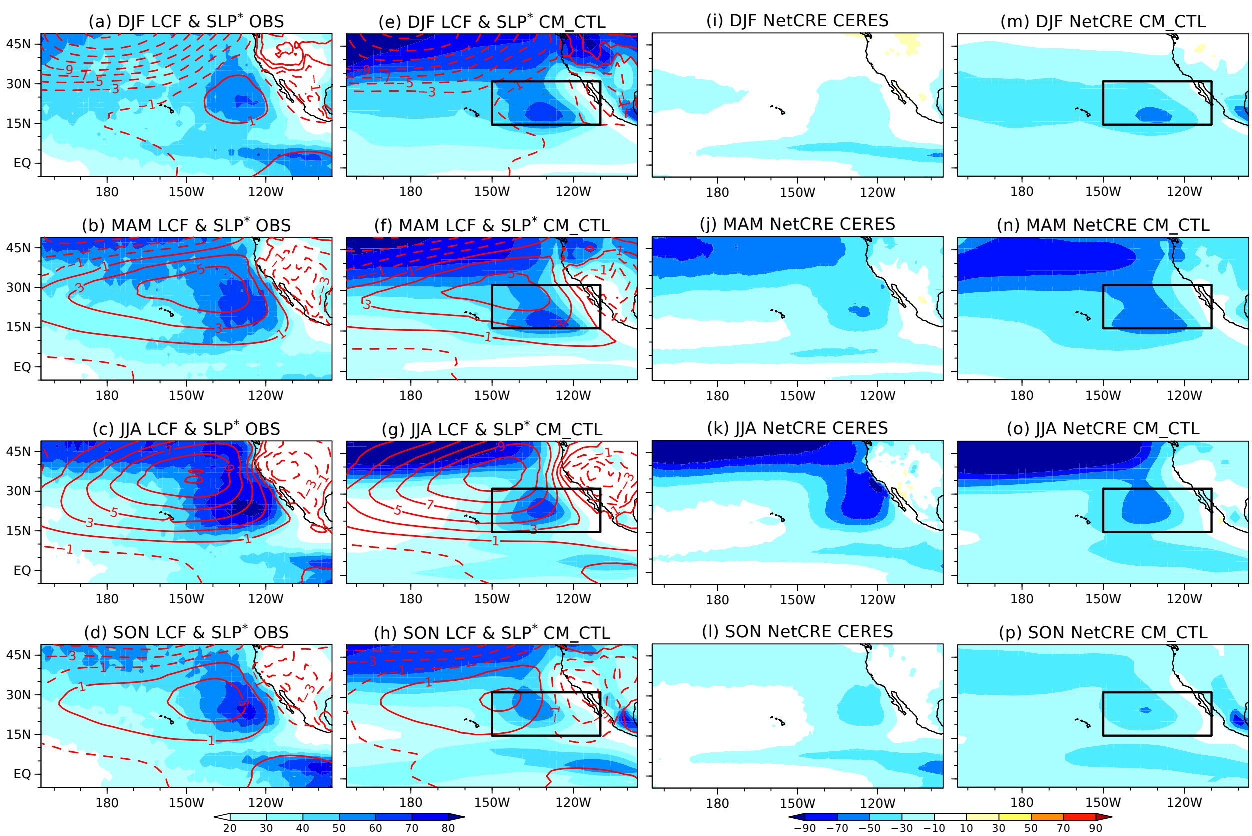

FIG. 2. (a)-(d) Climatological-mean distributions of CALIPSO-GOCCP LCF (%; color shaded as indicated at the bottom) and JRA-55 zonally asymmetric SLP (contoured for ±1, ±3, ±5 hPa; positive and negative values for solid and dashed lines, respectively) in (a) DJF, (b) MAM, (c) JJA, and (d) SON. (e)-(h) As in (a)-(d), respectively, but for the CM_CTL simulation. (i)-(l) As in (a)-(d), but for CERES-EBAF TOA net CRE (W m^{-2}). (m)-(p) As in (i)-(l), respectively, but for the CM_CTL simulation. Black box denotes the domain where low clouds are made transparent in CM_NoCRE.

TABLE 1. Overview of the CM2.1 (top two) and AM2.1 (bottom three) experiments.

	Radiative effects of Californian low clouds (150°W-110°W, 16°N-32°N)	Prescribed SST
CM_CTL	Active	—
CM_NoCRE	Inactive	—
AM_CTL	Active	Monthly climatology of CM_CTL
AM_NEPsst	Active	Monthly climatology of CM_NoCRE over the northeastern Pacific (180°-110°W, 10°N-32°N) and CM_CTL elsewhere
AM_NoCRE_sstFixed	Inactive	Monthly climatology of CM_CTL

b. Observational data

For the purpose of model validation, CM_CTL is compared with monthly observational data. We use the Japanese 55-year Reanalysis of the global atmosphere (JRA-55; Kobayashi et al. 2015; Harada et al. 2016) from 1979 to 2018 for sea-level pressure (SLP), the Clouds and the Earth's Radiant Energy System (CERES) Energy Balanced and Filled (EBAF) edition 4.1 (NASA/LARC/SD/ASDC 2019) from March 2000 to February 2020 for TOA radiative fluxes, the GCM-Oriented CALIPSO (*Cloud-Aerosol Lidar and Infrared Pathfinder Satellite Observations*) Cloud Product (GOCCP) version 3 (Chepfer et al. 2010) from June 2006 to May 2020 for LCF, and the Optimum Interpolation SST V2 (OISST; Reynolds et al. 2002) from 1982 through 2021 for SST. The horizontal resolution is 1.25° in JRA-55, 2° in CALIPSO-GOCCP, and 1° in CERES-EBAF and OISST.

Over the NEP, maximum negative CRE occurs off California associated with local LCF maximum (Fig. 2). These distributions compare well with the satellite observations, although their seasonal cycle in CM_CTL is weaker than in the observations. In addition, CM2.1 significantly underestimates low clouds along the California coast. Bias in the NEP SST is largely small but the coastal region suffers from warm SST bias (Fig. S1). The effect of the model bias will be discussed in Section 5. The North Pacific subtropical high represented as positive zonally asymmetric SLP is also well reproduced (Figs. 2a-h). Wittenberg et al. (2006) describe the tropical Pacific climate simulated by CM2.1.

3. Low-cloud impacts on the northeastern Pacific climate

a. Coupled response of SST and surface winds

We begin with the annual-mean coupled response to radiative forcing of low clouds over the NEP. Figure 3 shows annual-mean response of SST, surface winds, and SLP. In the NEP box, negative SST response is up to $-3°C$ (Fig. 3a) due to the negative CRE of low clouds (Figs. 2m-p), explaining local SST minima over the NEP. For example, at 20°N, the SST difference between 180° and 130°W increases from 0.2°C in CM_NoCRE to 2.4°C in CM_CTL. The SST response is not limited to the NEP box but extends well outside in the southwestward direction. The extension of the negative SST response is collocated with the strengthened northeasterly trade winds (Fig. 3a) associated with +2-hPa SLP response in the equatorward portion of the North Pacific subtropical high (Fig. 3b). The trade winds promote turbulent heat loss from the ocean by augmented wind speed and cold-air advection. The collocation of the negative SST anomalies and strengthened trade winds suggests the WES feedback. This coupled pattern is reminiscent of the North Pacific meridional mode (NPMM; Chiang and Vimont 2004), a coupled interannual variability of the NEP SST and surface winds characterized by negative SST anomalies and strengthened trade winds extending southwestward from the NEP. The NPMM stems from the WES feedback but low-cloud feedback can amplify it as the joint WES-low cloud feedback (Bellomo et al. 2014; Middlemas et al. 2019; Yang et al. 2023; Xie 2023).

Figures 4a-d show seasonal cycle of the coupled response. The horizontal pattern of the coupled response is similar throughout the year but the amplitude varies significantly. Under the enhanced negative CRE in spring and summer (Figs. 2m-p), the negative SST response in the NEP box maximizes in summer (Fig. 4c) as detailed in the next subsection. The trade wind and SST response extending outside the NEP box also maximize in summer, suggestive of the stronger WES feedback (Fig. 4c). Asymmetrically to spring, the strong trade wind response continues in autumn while the SST response starts to decay (Figs. 4d). Mechanisms of the surface wind response are discussed in Section 3c.

It is noteworthy that there are weak negative SST and surface easterly responses in the equatorial Pacific (Figs. 3a and 4a-d; its broader version with color shadings for positive values is shown in Fig. S2), reminiscent of the influence of the NPMM on ENSO. As reviewed by Amaya (2019), the NPMM's cool SST anomalies in the NEP can produce a La Niña-like SST pattern by forcing oceanic equatorial Kelvin waves and discharge of subsurface heat content. Indeed, impacts of the NEP low clouds on the equatorial Pacific have been identified by Yang et al. (2023) in interannual variations. Further investigation of the low-cloud impact on the equatorial Pacific is left for future work.

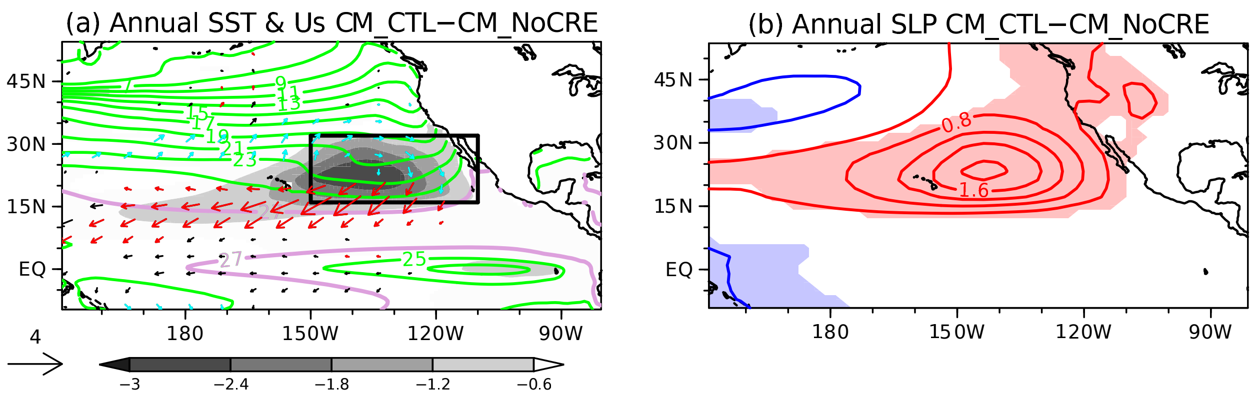

FIG. 3. Annual-mean response to CRE imposed in the black NEP box, represented by the difference defined as CM_CTL−CM_NoCRE. (a) SST (°C; shaded as indicated at the bottom; only points with the 99% confidence for the difference are shaded) and surface winds (m s^{-1}; arrows with reference on the left; red and blue arrows signify increased and decreased scalar wind speed, respectively, with the 99% confidence for the difference). Superimposed with green contours is climatological-mean SST (every 2°C with 27 °C isotherms in purple) in CM_CTL. Black box denotes the domain where low clouds are made transparent in CM_NoCRE. (b) SLP (every 0.4 hPa; red and blue lines for positive and negative values, respectively; zero lines are omitted). Color shading indicates the 99% confidence for the difference.

b. Ocean mixed-layer heat budget analysis

Ocean mixed-layer heat budget analysis supports the importance of shortwave and wind effects in the SST response. As in Xie et al. (2010), the budget equation for mixed-layer temperature (MLT) may be cast as

$$\left(\frac{\partial \mathrm{MLT}}{\partial t}\right)' = \left(\frac{F}{\rho c_p H}\right)' + D'_\mathrm{o} \qquad (1)$$

where primes denote anomalies defined as CM_CTL−CM_NoCRE. In (1), F, ρ, and c_p denote the net surface heat flux (NSHF; positive values for downward flux), sea-water density (1026 kg m^{-3}),

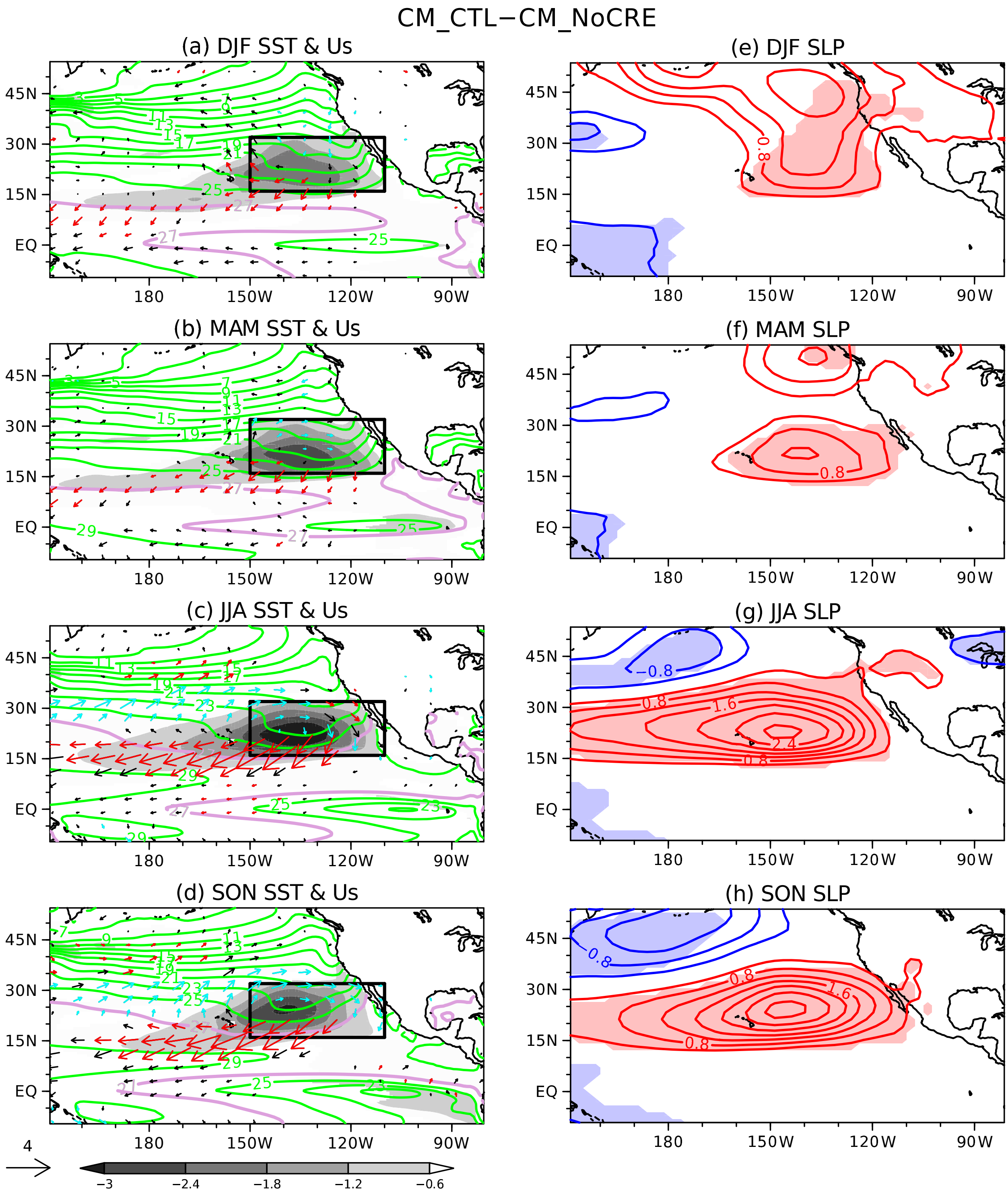

FIG. 4. As in Fig. 3, but for (a,e) DJF, (b,f) MAM, (c,g) JJA, and (d,h) SON.

and specific heat (3990 J kg^{-1} °C^{-1}), respectively, whereas H represents MLD. MLD is defined as a depth at which buoyancy difference is 0.0003 m s^{-2} relative to the surface. To this depth, water is well mixed so that MLT is equivalent to SST. For shortwave heat flux, we subtracted penetrating flux at the base of the mixed layer. D'_{o} is the effect of anomalous ocean heat transport due to three-dimensional advection and mixing (including entrainment at the base of the mixed layer), which is evaluated as the residual. The first term on the RHS of (1) can be linearly decomposed as

$$\left(\frac{F}{\rho c_p H}\right)' = \frac{F'}{\rho c_p \overline{H}} - \frac{\overline{F} \cdot H'}{\rho c_p \overline{H}^2}, \tag{2}$$

where overbars signify monthly climatologies in CM_NoCRE. The first term on the RHS of (2) represents the effects of anomalous NSHF under the reference climatology of MLD. The second term represents the effects of anomalous MLD under the reference climatology of F. For example, anomalously deeper MLD ($H' > 0$), which has larger mixed-layer heat capacity than a reference state, weakens the effect of climatological heating/cooling (e.g., Morioka et al. 2012; Amaya et al. 2021).

NSHF consists of shortwave (SW), longwave (LW), sensible heat (SH), and latent heat (LH) components ($F = F_{\mathrm{SW}} + F_{\mathrm{LW}} + F_{\mathrm{SH}} + F_{\mathrm{LH}}$). Due to the dependency of latent heat flux on SST, F'_{LH} is a mixture of atmosphere-driven and SST-driven components (Xie et al. 2010). Following bulk formula, SST-driven anomalous flux ($F^{\mathrm{o}'}_{\mathrm{LH}}$) may be cast as

$$F^{\mathrm{o}'}_{\mathrm{LH}} = \overline{F_{\mathrm{LH}}} \left(\frac{1}{\overline{q}_s} \frac{\mathrm{d}q_s}{\mathrm{d}T}\right) \mathrm{SST}' \tag{3}$$

where T and q_s are temperature and the saturation specific humidity following the Clausius-Clapeyron equation, respectively (Du and Xie 2008). This term represents the negative feedback on SST (e.g., negative SST′ yields less upward latent heat flux to warm the SST). The residual of anomalous LH represents the atmosphere-driven component ($F^{\mathrm{a}'}_{\mathrm{LH}}$) related to anomalous atmospheric conditions (wind speed, relative humidity, and difference between SST and surface air temperature),

$$F^{\mathrm{a}'}_{\mathrm{LH}} = F'_{\mathrm{LH}} - F^{\mathrm{o}'}_{\mathrm{LH}}. \tag{4}$$

Thus, the heat budget equation used in this study may be expressed as

$$\left(\frac{\partial \mathrm{MLT}}{\partial t}\right)' = \frac{F'_{\mathrm{SW}}}{\rho c_p \overline{H}} + \frac{F'_{\mathrm{LW}}}{\rho c_p \overline{H}} + \frac{F'_{\mathrm{SH}}}{\rho c_p \overline{H}} + \frac{F^{\mathrm{a}'}_{\mathrm{LH}}}{\rho c_p \overline{H}} + \frac{F^{\mathrm{o}'}_{\mathrm{LH}}}{\rho c_p \overline{H}} - \frac{\overline{F} \cdot H'}{\rho c_p \overline{H}^2} + D'_{\mathrm{o}}. \tag{5}$$

Figure 5 shows annual-mean contributions of individual terms in RHS of (5). Note that the time tendency (LHS of (5)) is negligible in the annual-mean response. The most prominent term within the NEP box is shortwave cooling by low clouds (F'_{SW}; Fig. 5a), which is partially offset by longwave radiation emitted from the low-cloud base (F'_{LW}; Fig. 5b). The atmosphere-driven component of latent heat flux ($F^{\mathrm{a}'}_{\mathrm{LH}}$) indicates its cooling effect in the equatorward portion of the NEP that extends southwestward outside the NEP box (Fig. 5d). This supports the presence of the WES feedback discussed in the preceding subsection. In response to the radiation and wind forcing, SST is lowered to reduce SST-driven latent heat supply (i.e., positive $F^{\mathrm{o}'}_{\mathrm{LH}}$ response in Fig. 5e). Another major damping arises from the anomalous ocean heat transport (D'_{o}; Fig. 5g), which is probably attributable in part to warm poleward Ekman advection due to the enhanced trade winds (Fig. 3a). The damping effect of the ocean heat transport associated with the low-cloud radiative effect is consistent with Middlemas et al. (2019).

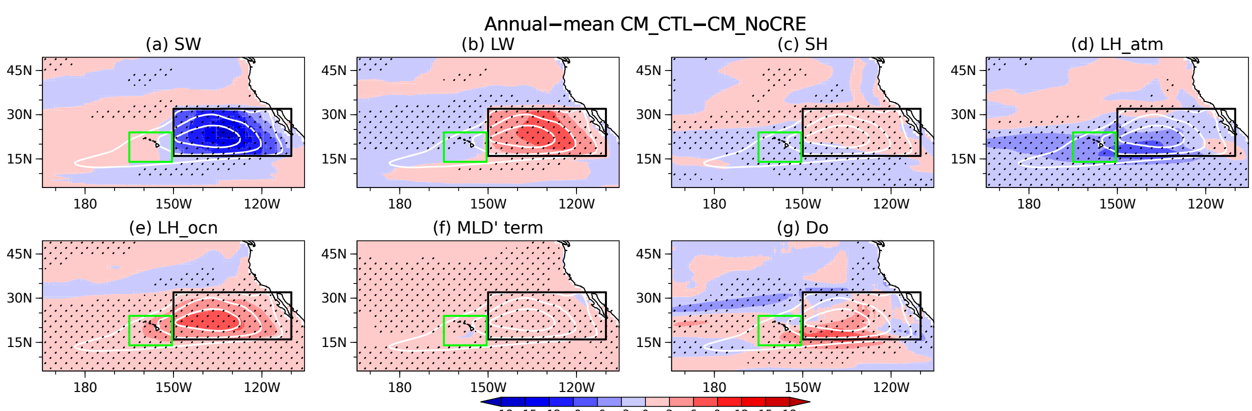

FIG. 5. Ocean mixed-layer heat budget (K yr^{-1}) for the annual-mean difference defined as CM_CTL−CM_NoCRE. (a) $F'_{\mathrm{SW}}/\rho c_p \overline{H}$, (b) $F'_{\mathrm{LW}}/\rho c_p \overline{H}$, (c) $F'_{\mathrm{SH}}/\rho c_p \overline{H}$, (d) $F^{\mathrm{a}'}_{\mathrm{LH}}/\rho c_p \overline{H}$, (e) $F^{\mathrm{o}'}_{\mathrm{LH}}/\rho c_p \overline{H}$, (f) $-\overline{F} \cdot H'/\rho c_p \overline{H}^2$, and (g) D'_{o}. Supperimposed with white contours is annual-mean SST response (−0.8, −1.6, and −2.4°C). Black and green boxes denotes the domains for the heat budget analysis in Fig. 6. Stippling indicates the 99% confidence for the difference.

Figure 6a shows seasonal cycle of the MLT (SST) response within the NEP box. The negative SST response develops from spring to summer. Despite slight offset by longwave radiation, this development is mostly attributable to shortwave cooling by low clouds (purple line in Fig. 6b) under climatologically shallow MLD in summer (Fig. 6c; comparison with observed MLD in Fig. S3). After the maximum of shortwave forcing in early summer, the SST effect on latent heat flux dominates to damp the SST response (brown dashed line in Fig. 6b).

By contrast, the box near Hawaii (165°W-150°W, 14°N-24°N; green rectangles in Fig. 5) is dominated by wind forcing. Here, the negative MLT response maximizes in summer as in the NEP box (Fig. 6d). However, despite small cooling in late spring, anomalous shortwave radiation is even positive in late summer (purple line in Fig. 6e) due to the decrease in deep precipitating clouds (see Section 3c). Rather, the summertime cooling is induced by atmosphere-driven latent heat flux (brown solid line in Fig. 6e), which supports the importance of the WES feedback. Additionally, the cooling effect of anomalous MLD (red line in Fig. 6e) acts to prolong the summertime MLT minimum. Anomalously deeper MLD (Fig. 6f) reduces the SST response to the climatological surface heating ($\overline{F}$) that is positive in summer following annual cycle of insolation (Fig. 6f). The deepening of MLD is probably due to wind-forced mixing and evaporative cooling by the enhanced trade winds (Niiler and Kraus 1977). As in the NEP box, the ocean heat transport and SST-driven latent heat flux (blue solid and brown dashed lines in Fig. 6e) act to damp the SST cooling.

In summary, the mixed-layer heat budget analysis supports the importance of both the radiative and wind effects on the SST cooling. The strong shortwave cooling by low clouds dominates the SST cooling in the low-cloud region whereas the wind forcing explains its southwestward expansion. These processes develop in concert to form the maximum SST response in summer.

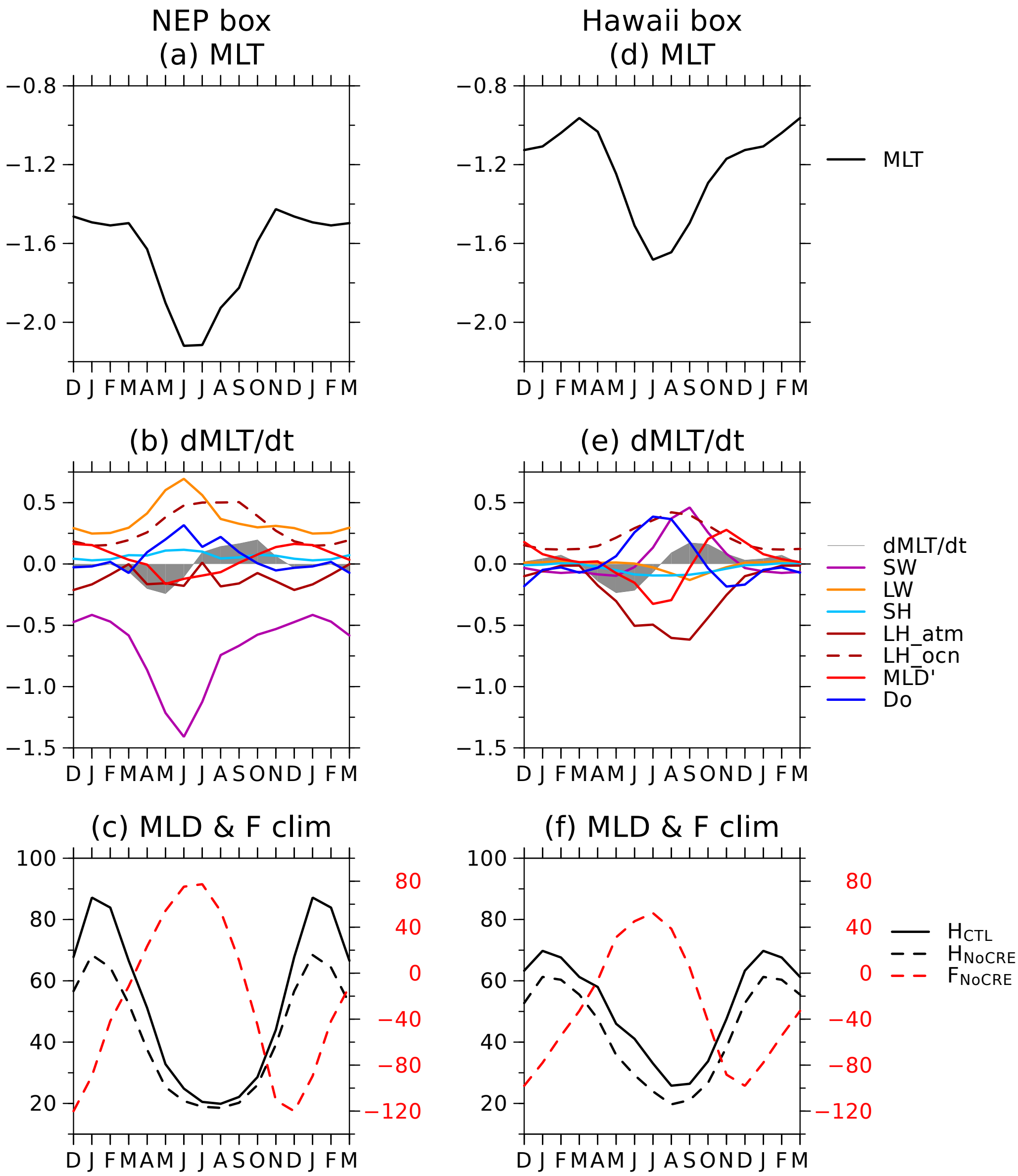

FIG. 6. Seasonal cycle of mixed-layer quantities averaged over (a)-(c) the NEP box (black rectangles in Fig. 5) and (d)-(f) the Hawaii box (green rectangles in Fig. 5). (a)(d) MLT response (°C). (b)(e) Time tendency of MLT response ($\partial \mathrm{MLT}/\partial t$; grey filled line) and its decomposition into shortwave radiation ($F'_{\mathrm{SW}}/\rho c_p \overline{H}$; purple), longwave radiation ($F'_{\mathrm{LW}}/\rho c_p \overline{H}$; orange), sensible heat flux ($F'_{\mathrm{SH}}/\rho c_p \overline{H}$; light blue), atmosphere-driven latent heat flux ($F^{a'}_{\mathrm{LH}}/\rho c_p \overline{H}$; brown solid), SST-driven latent heat flux ($F^{o'}_{\mathrm{LH}}/\rho c_p \overline{H}$; brown dashed), anomalous MLD effect ($-\overline{F} \cdot H'/\rho c_p \overline{H}^2$; red), and ocean heat transport effect (D'_{o}; blue) in (5). Unit is °C (30 day)$^{-1}$. (c)(f) Monthly climatology in CM_NoCRE of net surface heat flux ($\overline{F}$; unit is W m^{-2}; red dashed) and MLD ($\overline{H}$; unit is m; black dashed). Black solid line indicates monthly climatology of MLD (m) in CM_CTL. The panels show one year starting from December, and four additional months ending in March.

c. Response of the North Pacific subtropical high and its mechanism

In this subsection, the surface anticyclonic response and its seasonal difference are investigated in detail. This type of the response is often regarded simply as part of the WES feedback (Bellomo et al. 2014; Middlemas et al. 2019; Yang et al. 2023), but it has not been clarified whether it stems from cloud-top longwave cooling (Miyasaka and Nakamura 2005, 2010), reduced deep-convective heating (Miyamoto et al. 2021), or reduced sensible heating from the ocean.

Figures 4e-h show the seasonal-mean response of SLP in CM2.1. The subtropical center of the positive response is located at (150°-160°W, 20°-25°N) with minimum (~1.2 hPa) in spring and its maximum (~3 hPa) in summer and autumn. It coincides with the equatorward portion of the North Pacific subtropical high (Figs. 2e-h). We note that the winter response extends poleward, but its poleward portion exhibits weak statistical significance. The equatorward portion of the wintertime response is comparable to its springtime counterpart. Thus, the strong SLP response in summer and autumn is important for the annual-mean response (Fig. 3b).

Mechanisms of the SST forcing on the subtropical SLP response can be inferred from in-atmosphere diabatic heating. Figure 7 shows the vertically integrated response of diabatic heating, which is decomposed into condensation (Q_{precip}), vertical diffusion (Q_{vdf}), and radiation (Q_{rad}) components. The most prominent feature is seasonality in the Q_{precip} response (Figs. 7a-d). In summer and autumn, strong cooling response extends westward from the equatorward portion of the low-cloud deck, with narrower heating to the south. Since the vertically integrated Q_{precip} response is virtually equivalent to precipitation response, the summer and autumn responses indicate southward shift and shrink of the ITCZ, which is centered at 5°N-10°N (Wittenberg et al. 2006). Mid-tropospheric diabatic cooling induces anomalous surface anticyclone to the west of the cooling, which is known as a Matsuno-Gill-type baroclinic Rossby-wave response in the equatorial wave theory (Matsuno 1966; Gill 1980; Kraucunas and Hartmann 2007). Thus, the Q_{precip} cooling reinforces the subtropical high (Figs. 4g-h). An additional contribution comes from the moderate Q_{rad} cooling (Figs. 7k-l). Note that, as illustrated in Voigt et al. (2021), vertically integrated Q_{rad} within the atmosphere does not include ocean surface heating/cooling by clouds, which is dominant in TOA CRE. The Q_{rad} cooling comes from the reduction of high clouds of the ITCZ that induce longwave heating below the cloud base as well as increased low clouds that induce longwave cooling from their tops (Voigt et al. 2021). Reflecting the negative SST response that acts to decrease sensible heating from the ocean, the $Q_{\rm vdf}$ response is negative throughout the year but very weak (Figs. 7e-h). In winter and spring, the pronounced $Q_{\rm precip}$ cooling diminishes (Figs. 7a-b) despite the comparable $Q_{\rm rad}$ remaining as in summer and autumn within the low-cloud region (Figs. 7i-j), This seasonality in the $Q_{\rm precip}$ cooling is consistent with the stronger positive SLP response in summer and autumn (Figs. 4e-h). Thus, the precipitation response is key to the seasonality in the subtropical anticyclonic response, as found for the Mascarene high over the South Indian Ocean (Miyamoto et al. 2021, 2022a).

This precipitation decrease is tied to the negative SST response. In Figs. 7a-d, superimposed with contours are isotherms of convective threshold SST (27°C), which corresponds to the threshold for active deep convection (Graham and Barnett 1987). We note that, although the climatological precipitation is overestimated, precipitation dependency on the underlying SST over the NEP is well reproduced in CM2.1 (Fig. S4). In summer and autumn, the 27°C isotherm advances farther northward into the low-cloud region in CM_NoCRE than in CM_CTL. The low-cloud-induced negative SST response (Figs. 4c-d) markedly reduces precipitation with the pronounced $Q_{\rm precip}$ decrease over the equatorward portion of the negative SST response (Figs. 7c-d). As the SST decrease extends into the deep tropics mainly through the WES feedback, the area of the negative $Q_{\rm precip}$ response also expands southwestward through Hawaii in summer and autumn. By contrast, displacement of the 27°C isotherms between the CM2.1 experiments is relatively small in winter and spring (Figs. 7a-b) due not only to the weaker SST response (Figs. 4a-b) but also to lower climatological SST after the winter solstice. This results in the much weaker $Q_{\rm precip}$ decrease in winter and spring.

The importance of the air-sea coupling over the NEP is substantiated by the atmosphere general circulation model (AGCM) experiments (Fig. 8). As evident from the comparison between the AM_CTL and AM_NoCRE_sstFixed experiments, the CRE impact on summertime SLP without SST changes is quite weak (Fig. 8b) compared with its CM2.1 counterpart (Fig. 4g). This is consistent with the weak Q cooling due to the lack of the precipitation decrease south of the NEP box (Fig. 8d). Forcing an atmospheric dynamical model with zonally asymmetric radiative cooling obtained from an atmospheric reanalysis, Miyasaka and Nakamura (2005) argued that the formation of the summertime North Pacific subtropical high is explained mainly as the response to longwave cooling from low clouds. However, as discussed in Miyamoto et al. (2021), cloud-top longwave cooling of low clouds is mostly compensated by Q_{precip} and Q_{vdf} heating. Thus, low-cloud impacts on the subtropical high without air-sea couplings are rather weak, consistent with the AGCM experiments by Kawai and Koshiro (2020).

By contrast, in response to the imposed SST cooling in the NEP, the difference of AM_CTL from AM_NEPsst well reproduces the summertime enhanced subtropical high and decreased Q ($Q_{\text{precip}} + Q_{\text{vdf}} + Q_{\text{rad}}$) simulated in CM2.1 despite their overestimation (Figs. 8a and 8c). We have confirmed that the remote influence of the equatorial Pacific SST anomalies (10°S-10°N) on the subtropical high is weak, as verified by another AM2.1 experiment forced with them (Fig. S5). Seasonal cycle of the SLP and Q responses in CM2.1 is also mostly explained by those of the NEP SST cooling (Figs. S6-8). Overall, our analysis demonstrates the importance of the subtropical air-sea coupling in the non-local low-cloud feedback.

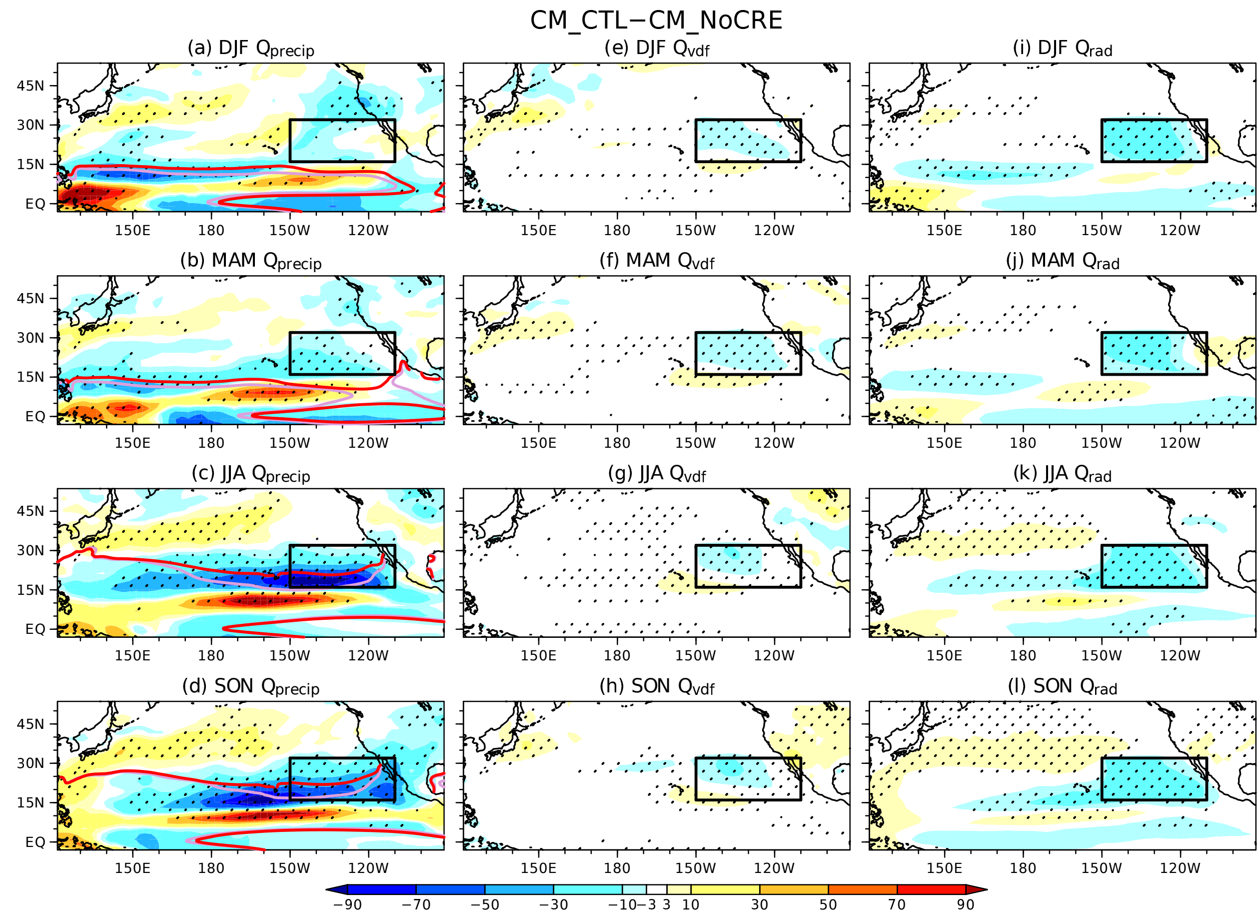

FIG. 7. Response to CRE imposed in the black NEP box, represented by the difference defined as CM_CTL−CM_NoCRE. (a)-(d) vertically integrated Q_{precip} (W m^{-2}; color shaded as indicated at the bottom) in (a) DJF, (b) MAM, (c) JJA, and (d) SON. (e)-(h) As in (a)-(d), respectively, but for Q_{vdf}. (i)-(l) As in (a)-(d), respectively, but for Q_{rad}. Stippling indicates the 99% confidence for the difference. Black box denotes the domain where low clouds are made transparent in CM_NoCRE. In (a)-(d), superimposed with purple and red contours are climatological-mean 27°C SST isotherms in CM_CTL and CM_NoCRE, respectively.

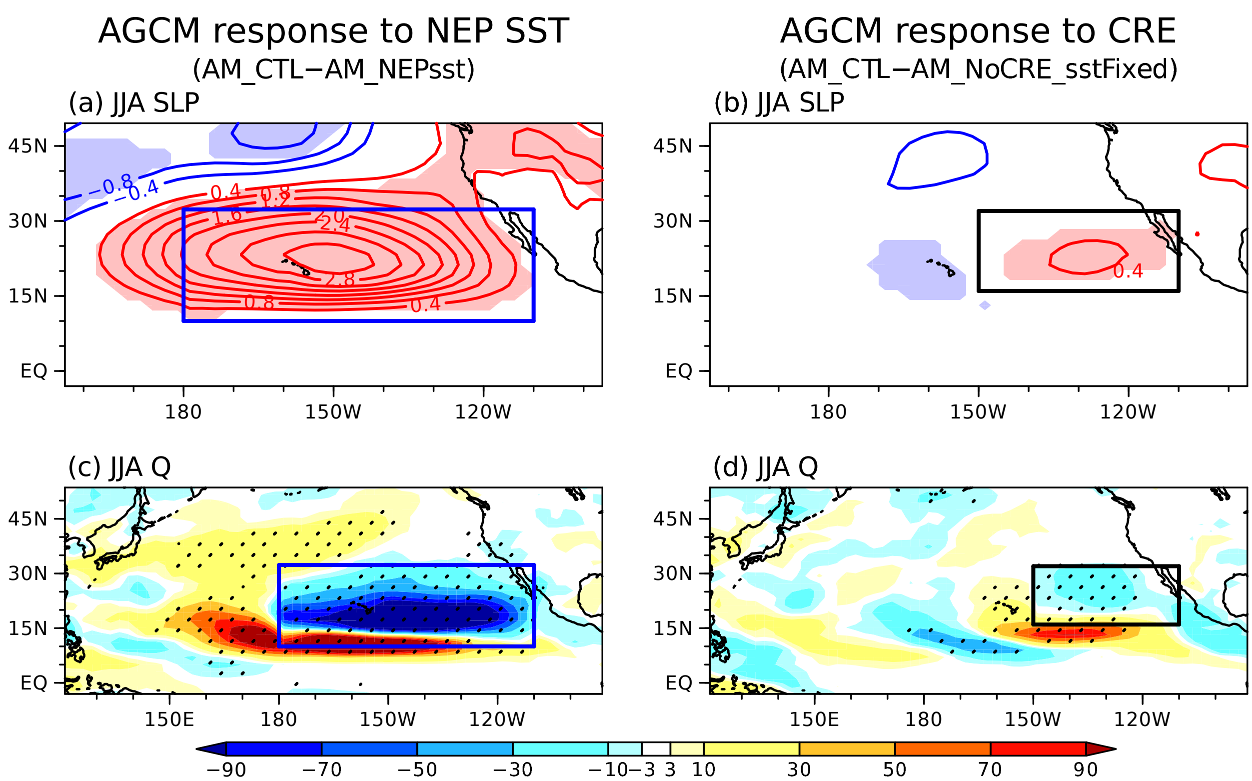

Fig. 8. AM2.1 response in JJA to (a)(c) anomalous SST over the NEP and (b)(d) CRE without SST changes. (a)(c) Differences defined as AM_CTL−AM_NEPsst in climatological-mean (a) SLP (every 0.4 hPa; red and blue lines for positive and negative values, respectively; zero lines are omitted) and (c) $Q_{\mathrm{precip}} + Q_{\mathrm{vdf}} + Q_{\mathrm{rad}}$ (W m^{-2}; color shaded as indicated at the bottom). Color shading in (a) and stippling in (c) indicate the 99% confidence for the difference. Blue box denotes the domain where SST anomalies are prescribed in AM_NEPsst. (b)(d) As in (a) and (c), respectively, but for AM_CTL−AM_NoCRE_sstFixed. Black box denotes the domain where low clouds are transparent in AM_NoCRE_sstFixed.

4. Discussions

a. Three-dimensional structure of the atmospheric response and its implication on tropical cyclone activity around Hawaii

The low-cloud impact extends into the upper troposphere. Here, we focus on the response from June through November (JJASON), i.e., the hurricane season over the NEP (Gray 1968). As shown in Fig. 9, CM2.1 simulates upper-tropospheric cyclonic response above the surface anticyclonic response over the summertime NEP. This first baroclinic structure as observed climatologically over the equatorward portion of the subtropical high (Miyasaka and Nakamura 2005; Nakamura et al. 2010), is consistent with the baroclinic Matsuno-Gill-type response to the anomalous diabatic cooling (Figs. 7c,k). As shown in Fig. 9, the low-cloud impact reaches Western Europe as wave trains from the NEP. Wave-activity flux, which is parallel to the group velocity of stationary Rossby waves (Takaya and Nakamura 2001), indicates the eastward wave propagation through subpolar North America and the Atlantic, as actually observed climatologically in summer (Miyasaka and Naakmura 2005). This response is also reproduced by AM2.1 experiments forced by anomalous NEP SST (AM_CTL-AM_NEPsst; figure not shown).

This first baroclinic structure corresponds to the enhanced vertical wind shear (VWS) on the southern flank of the subtropical high. Figure 10a shows climatological VWS in JJASON, which is evaluated as a difference in monthly-mean zonal and meridional wind components between the 200-hPa and 850-hPa levels:

$$\mathrm{VWS} = \sqrt{(u_{200} - u_{850})^2 + (v_{200} - v_{850})^2}. \tag{6}$$

It features enhanced VWS between the near-surface easterlies and upper-tropospheric westerlies over Hawaii. Since VWS is destructive to tropical cyclones (Gray 1968; Tang and Emanuel 2012), this VWS prevents powerful hurricanes from hitting Hawaii.

Although the horizontal resolution of CM2.1 is insufficient to simulate tropical cyclones, it is beneficial to discuss the low-cloud impact on tropical cyclone genesis through environmental factors. The VWS response to CRE is shown in Fig. 10b. It exhibits positive VWS response on the southern flank of the upper-tropospheric cyclonic response, which accounts for ~30% of the climatological VWS around Hawaii in CM_CTL. The negative SST response also acts to decrease hurricane genesis over the NEP. The response of the maximum potential intensity for tropical cyclones (MPI; Emanuel 1988) shown in Fig. 10c features the negative MPI response that maximizes over the low-cloud regions and extends southwestward through Hawaii, in accordance with the negative SST response. The tropical cyclone genesis around Hawaii is further decreased by negative response of mid-tropospheric relative humidity (Fig. 10d). This drying is associated with anomalous subsidence owing to the suppression of deep-convective precipitation under the lowered SST, as discussed in the preceding section.

Collective influence of the environmental factors is evaluated with the genesis potential index (GPI; Camargo et al. 2007), which may be cast as

$$\mathrm{GPI} = |10^5\zeta|^{1.5}\left(\frac{\mathrm{RH}}{50}\right)^3\left(\frac{\mathrm{MPI}}{70}\right)^3(1+0.1\mathrm{VWS})^{-2} \tag{7}$$

where ζ, RH, and MPI are 850-hPa relative vorticity (s^{-1}), 600-hPa relative humidity (%), and the maximum potential intensity ($\mathrm{m\ s}^{-1}$). The GPI response shown in Fig. 10e features zonally elongated negative response maximized just south of Hawaii, which corresponds to reduced hurricane genesis. The relative contribution to this GPI response is derived by taking the natural logarithm of (7):

$$(\log\mathrm{GPI})' = 1.5(\log|10^5\zeta|)' + 3\left[\log\left(\frac{\mathrm{RH}}{50}\right)\right]' + 3\left[\log\left(\frac{\mathrm{MPI}}{70}\right)\right]' - 2\left[\log(1+0.1\mathrm{VWS})\right]' \tag{8}$$

Decomposition of the GPI response based on (8) reveals that the RH, VWS, and MPI terms explain 42%, 30%, and 20% of the total response, respectively (Fig. 10f). The vorticity term plays a minor role. The analysis suggests that Californian low clouds act to protect Hawaii from hurricanes by lowering SST, drying the mid-troposphere, and increasing VWS.

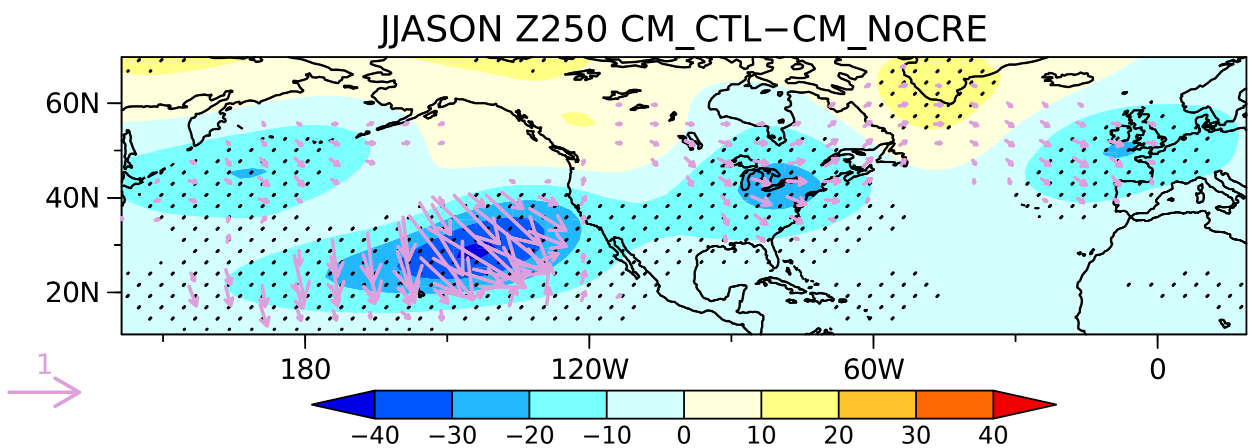

FIG. 9. JJASON 250-hPa geopotential height response (m) to CRE imposed in the black NEP box, represented by the difference defined as CM_CTL−CM_NoCRE. Here, the global-mean response has been subtracted to eliminate signal of global cooling. Stippling indicates the 99% confidence for the difference. Superimposed with arrows is wave activity flux for stationary Rossby waves ($m^2\ s^{-2}$; reference on the left) formulated by Takaya and Nakamura (2001). Only fluxes above 0.05 $m^2\ s^{-2}$ in the westerly regions are drawn.

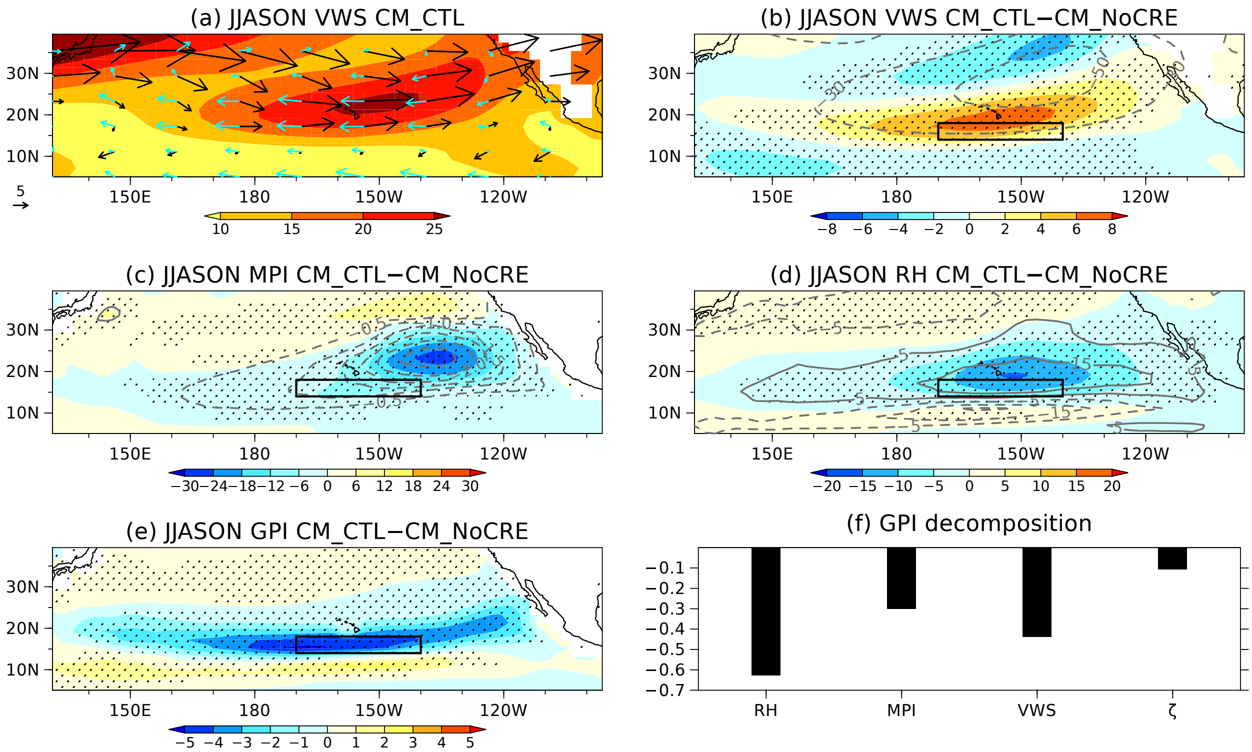

FIG. 10. (a) JJASON climatology of VWS (color shaded for every 5 m s^{-1}) in CM_CTL. Superimposed with black and blue arrows are JJASON climatologies of 200-hPa and 850-hPa winds in CM_CTL, respectively. (b) JJASON difference (defined as CM_CTL−CM_NoCRE) in VWS (color shaded for every 2 m s^{-1}) and 200-hPa geopotential height (contoured for ±10, ±30, ±50 ... m; positive and negative values for solid and dashed lines, respectively). (c) As in (b), but for MPI (color shaded for every 6 m/s) and SST (contoured for ±0.5, ±1, ±1.5 ... °C). (d) As in (b), but for 600-hPa relative humidity (color shaded for every 5%) and p-velocity (contoured ±5, ±15, ±25 ... hPa day^{-1}). (e) As in (b), but for GPI. (f) Decomposition of logGPI response to individual terms (RHS of (8)) averaged within black boxes in (b)-(e). In (b)-(e), stippling indicates the 99% confidence for the color-shaded difference.

b. Kuroshio acceleration and its influence on precipitation

The low-cloud impact extends farther into the northwestern Pacific through an ocean circulation change. Figure 11a shows the annual-mean CM2.1 response of wind stress curl and sea surface height (SSH). Associated with the positive SLP response (Figs. 4e-h), there is a strong anticyclonic wind stress curl response centered at 20°N, which is sandwiched meridionally by cyclonic responses (Fig. 11a). Forcing oceanic Rossby waves that propagate westward, this anticyclonic wind stress curl induces positive SSH response in the subtropical northwestern Pacific (Fig. 11a). This is indicative of acceleration of the subtropical gyre accompanied by the intensified North Equatorial Current and Kuroshio (Fig. 11b). The poleward and eastward current responses along Kuroshio and its extension account for ~30% of the CM_CTL current. Unlike the NEP SST response, this current response seems to be delayed by about five to ten years after the simulations are branched off (Fig. S9) due to the oceanic Rossby-wave propagations. Reflecting the enhanced heat transport, positive SST responses form along the accelerated Kuroshio and maximize its extension (Fig. 11b).

Recent studies have indicated that the Kuroshio Current system has significant impacts on the overlying atmosphere through heat and moisture supply (e.g., Seo et al. 2023). As shown in Fig. 11c, upward turbulent heat fluxes are enhanced (up to 20% of CM_NoCRE climatology) over the warm SST responses in the CM2.1 simulations, indicative of the oceanic forcing on the overlying atmosphere. Figure 11d shows the annual-mean response of precipitation and ∇^2SLP, the latter of which is proportional to surface wind convergence based on a marine boundary layer model (Lindzen and Nigam 1987; Minobe et al. 2008). Through hydrostatic pressure adjustments (Lindzen and Nigam 1987; Minobe et al. 2008), the enhanced sensible heating by the Kuroshio and its extension yields positive ∇^2SLP response locally (Fig. 11d). The associated enhancement of surface wind convergence as well as the augmented surface latent heat flux from the warmer SST increases precipitation by 10-20% of the CM_NoCRE climatology over the Kuroshio regions (Fig. 11d). This precipitation response is found in both warm and cold seasons (not shown). Such impacts of the warm Kuroshio SST on local precipitation have been identified in observations and reanalysis datasets (e.g., Tokinaga et al. 2009; Minobe et al. 2010; Masunaga et al. 2015, 2020). The Kuroshio warming may further energize atmospheric transient eddy activity (Taguchi et al. 2009) that acts to increase precipitation and to feed back onto the North Pacific subtropical high (Joh and Di Lorenzo 2019, and references therein), although it is not evident in our simulations (not shown) potentially due to the low resolution of the model. Thus, Californian low clouds can affect the climate in the Kuroshio region by accelerating the subtropical ocean gyre.

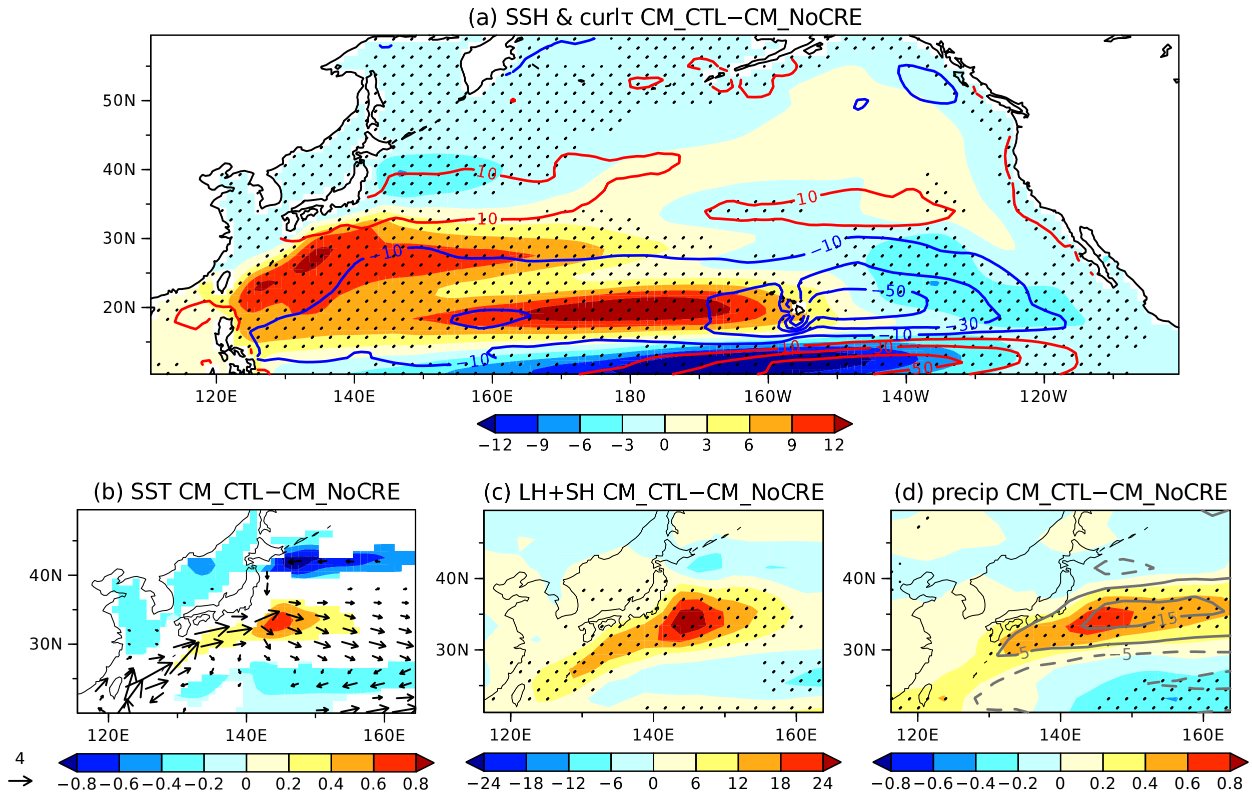

FIG. 11. Annual-mean response to CRE in the black NEP box, represented by the difference defined as CM_CTL−CM_NoCRE. (a) SSH (color shaded for every 3 cm) and wind stress curl (contoured for ±10, ±30, ±50 ... $\times 10^{-9}$ N m^{-3}; positive and negative values for red and blue lines, respectively). (b) SST (color shaded for every 0.2 °C) and surface current (cm s^{-1}; arrows with reference on the left) with the 99% confidence for the difference. (c) Turbulent heat flux (sensible and latent heat fluxes combined; color shaded for every 6 W m^{-2}; positive values for upward flux). (d) Precipitation (color shaded for every mm day^{-1}) and ∇^2SLP (contoured for ±5, ±15, ±25 ... $\times 10^{-13}$ hPa m^{-2}; positive and negative values for solid and dashed lines, respectively). In (a), (c), and (d), stippling indicates the 99% confidence for the color-shaded difference.

5. Concluding remarks

It has been suggested that low clouds not only induce local SST cooling but also induce non-local effects through cloud-top longwave cooling (Miyasaka and Nakamura 2005) and WES feedback

(Bellomo et al. 2014; Middlemas et al. 2019; Yang et al. 2023). By disabling CRE regionally in a fully coupled AOGCM, this study has demonstrated that the radiative effects of low clouds off the California coast have significant climatological impacts over the North Pacific. The negative CRE of low clouds causes a local SST decrease of up to 3°C on an annual average, contributing to the zonal SST minima over the NEP. Notably, the SST response is not limited to the low-cloud region but extends well outside in the southwestward direction. The extension of the negative SST response is collocated with the strengthened northeasterly trades associated with the enhanced subtropical high (+2-hPa response on an annual average), suggestive of the WES feedback.

We highlight that the atmospheric responses are much stronger in boreal summer and autumn than in winter and spring under the effect of background climatologies. The shortwave CRE strengthens toward summer due to large insolation. Combined with seasonally shallow MLD, the subtropical negative SST response maximizes in summer. This lowered SST suppresses deep-convective precipitation that would otherwise occur over seasonally high SST in the absence of CRE. Associated anomalous diabatic cooling induces the surface anticyclonic response as a baroclinic Matsuno-Gill pattern. The enhanced trade winds on its equatorward flank further cool SST through the WES feedback. Since climatological SST warming lags the summertime solstice, the precipitation and surface anticyclonic response remains strong in autumn after the SST response starts to decay, introducing spring-autumn asymmetries. No such enhancement of the atmospheric response in the warm seasons is simulated in the AGCM no-low-cloud experiments without SST changes, indicative of the crucial role of the air-sea interactions.

The aforementioned influence of Californian low clouds has implications on the climate over the Hawaii and Kuroshio regions. As a Matsuno-Gill-type Rossby-wave response to the diabatic cooling, the surface anticyclonic response accompanies an upper-tropospheric cyclonic response. This first baroclinic structure augments vertical wind shear between the near-surface trades and upper-level westerlies around Hawaii. This result implies that low clouds act to prevent hurricanes from reaching Hawaii by enhancing environmental vertical wind shear and lowering regional SST. Our simulations also suggest a remote influence of low clouds through oceanic teleconnection. Input of anticyclonic wind stress leads to acceleration of the North Pacific subtropical ocean gyre and associated SST increase along the Kuroshio and its extension. Enhanced upward surface heat and moisture fluxes, which manifest forcing from the warmed Kuroshio and its extension, act to increase precipitation locally.

As indicated in Section 2a, CM2.1 underestimates the seasonal enhancement of the negative CRE, biasing the simulated response to it. Figure 12 revisits the TOA CRE bias in the NEP box in CM2.1, with comparison to the CMIP6 coupled models. In CM2.1, the negative CRE is strongly overestimated in cold season (Fig. 12c) while slightly underestimated in warm season (Fig. 12b), resulting in the overestimated annual-mean negative CRE (Fig. 12a). This suggests that the response to the CRE in CM2.1 may be underestimated in summer but overestimated in winter. Nevertheless, the fact that the pronounced seasonal enhancement in the low-cloud impact is simulated despite the weaker seasonal cycle of low clouds in CM2.1 is a testament to its robustness. We also note that the summertime intensification of the low-cloud impact by seasonally high SST is similar to the low-cloud impact over the South Indian Ocean (Miyamoto et al. 2021, 2022a). The CMIP6 models tend to underestimate the annual-mean negative CRE but with large intermodel spread (Fig. 12a). Interestingly, the seasonality of the negative CRE also tends to be weak in the CMIP6 coupled models, with significant underestimation in warm season (Fig. 12b). This implies that the low-cloud impacts in warm season in the CMIP6 models might be underestimated, but other biases such as precipitation dependency on SST can complicate the problem. In addition, the low-cloud impacts along the California coast are missing in our simulations (Fig. 2). Thus, it is important to evaluate the low-cloud impacts in other climate models with care on the model biases. The key factors of the mechanisms identified in our study will help understand the low-cloud impacts simulated in other climate models in climatology, and possibly in climate variability and change under intermodel diversity of low cloud-SST feedback (Myers et al. 2018; Kim et al. 2022).

A suite of our AOGCM experiments indicates the significant non-local impacts of low clouds even under damping by ocean dynamics. This is in line with the recent studies on interannual variations (Burgman et al. 2017; Middlemas et al. 2019; Yang et al. 2023). Furthermore, the low-cloud impacts simulated in our model may be operative in the past and future climate change that accompanies persistent shortwave forcing of low clouds. For example, subtropical low clouds may decrease in response to CO_2 increase (e.g., Qu et al. 2014; Myers et al. 2021). Interestingly, satellite observations over the last two decades revealed a significant positive trend in the net downward radiation at the top of the atmosphere attributable primarily to decreasing low-cloud fraction over the subtropical Northeastern Pacific (Loeb et al. 2021, 2022). Nevertheless, our simulated climate without subtropical low clouds could happen in the past and future, since stratocumulus clouds have vulnerability and hysteresis against CO_2-level rises (Schneider et al. 2019). Our results also have implications for geoengineering by marine cloud brightening (e.g., Latham et al. 2008). Baughman et al. (2012) demonstrated that cloud brightening in the NEP low-cloud region yields non-local impacts with a southwestward extension of the SST cooling. Our analysis has revealed the dynamical mechanisms of this southwestward extension through the joint low cloud-WES feedback. Overall, our series of studies have demonstrated that low clouds play a key role in shaping a regional climate system by modulating subtropical air-sea interactions.

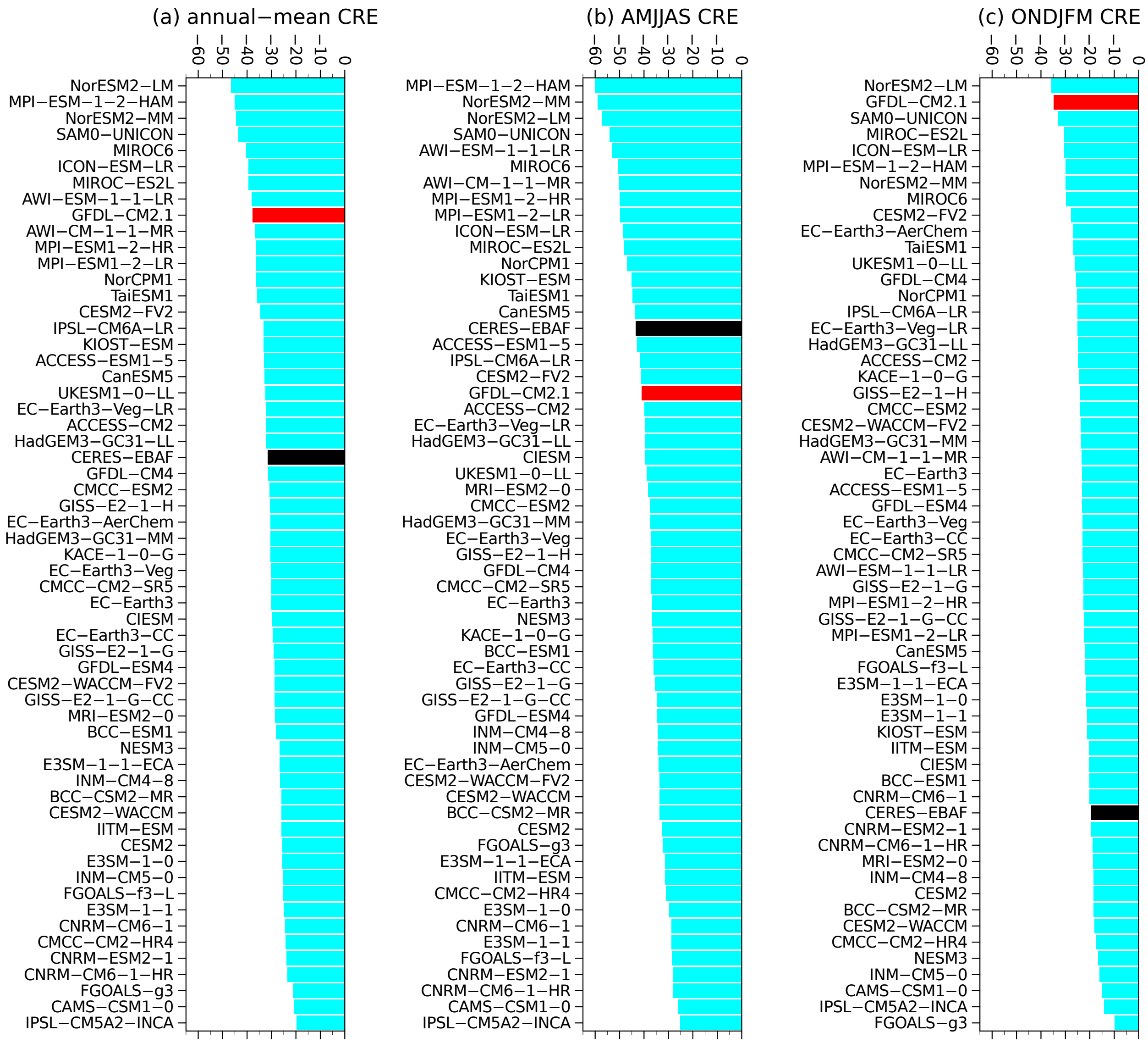

FIG. 12. Climatological TOA CRE in the NEP box (W m^{-2}) in CERES-EBAF (black), CM_CTL (red), and the CMIP6 historical simulations (light blue). (a) Annual, (b) AMJJAS (from April through September), and (c) ONDJFM (from October through March) averages.

Acknowledgments. We thank Hideaki Kawai and anonymous reviewers for their sound criticism and constructive feedback. We also thank Andrew Williams and Tadahiro Hayasaka for valuable input. This study is supported by the Japan Society for the Promotion of Science through Grants-in-Aid for Scientific Research (JP19H05702, JP19H05703, JP20H01970, JP22H01292, and JP23H01241), by the Japanese Ministry of the Environment through the Environment Research and Technology Development Fund (JPMEERF20222002), by the Japanese Ministry of Education, Culture, Sports, Science and Technology (MEXT) programs for the ArCS II (JPMXD1420318865) and the advanced studies of climate change projection (JPMXD0722680395), by the Japan Science and Technology Agency through COI-NEXT (JPMJPF2013), and by the National Science Foundation (AGS-1934392).

Data availability statement. The authors can provide the model simulation data upon reasonable requests. The observational data used in this study are available online (JRA-55: `https://jra.kishou.go.jp/JRA-55/index_en.html`; CALIPSO-GOCCP; `https://climserv.ipsl.polytechnique.fr/cfmip-obs/`; CERES-EBAF: `https://ceres.larc.nasa.gov/data/`; OISST: `https://psl.noaa.gov`; MILA-GPV: `https://www.jamstec.go.jp/argo_research/dataset/milagpv/mila_en.html`; TRMM: `https://disc.gsfc.nasa.gov/datasets/TRMM_3B42_7/summary`). The CMIP6 data can be obtained through the Earth System Grid Federation (ESGF) Data Portals. The maximum potential intensity of tropical cyclones is calculated with pyPI (Gilford 2021).

References

Amaya, D. J., 2019: The Pacific meridional mode and ENSO: A review. *Curr. Clim. Change Rep.*, **5**, 296–307, https://doi.org/10.1007/s40641-019-00142-x.

Amaya, D. J., M. A. Alexander, A. Capotondi, C. Deser, K. B. Karnauskas, A. J. Miller, and N. J. Mantua, 2021: Are long-term changes in mixed layer depth influencing North Pacific marine heatwaves? *Bull. Amer. Meteor. Soc.*, **34**, 59–66, https://doi.org/10.1175/BAMS-D-20-0144.2.

Baughman, E., A. Gnanadesikan, A. Degaetano, and A. Adcroft, 2012: Investigation of the surface and circulation impacts of cloud-brightening geoengineering. *J. Climate*, **25**, 7527–7543, https://doi.org/10.1175/JCLI-D-11-00282.1.

Bellomo, K., A. Clement, T. Mauritsen, and B. Stevens, 2014: Simulating the role of subtropical stratocumulus clouds in driving Pacific climate variability. *J. Climate*, **27**, 5119–5131, https://doi.org/10.1175/JCLI-D-13-00548.1.

Bony, S., and J.-L. Dufresne, 2005: Marine boundary layer clouds at the heart of tropical cloud feedback uncertainties in climate models. *Geophys. Res. Lett.*, **32**, L20806, https://doi.org/10.1029/2005GL023851.

Burgman, R. J., B. P. Kirtman, A. C. Clement, and H. Vazquez, 2017: Model evidence for low-level cloud feedback driving persistent changes in atmospheric circulation and regional hydroclimate. *Geophys. Res. Lett.*, https://doi.org/10.1002/2016GL071978.

Camargo, S. J., K. A. Emanuel, and A. H. Sobel, 2007: Use of a genesis potential index to diagnose ENSO effects on tropical cyclone genesis. *J. Climate*, **20**, 4819–4834, https://doi.org/10.1175/JCLI4282.1.

Chang, J. C. H., and D. J. Vimont, 2004: Analogous Pacific and Atlantic meridional modes of tropical atmosphere-ocean variability. *J. Climate*, **17**, 4143–4158, https://doi.org/10.1175/JCLI4953.1.

Chepfer, H., S. Bony, D. M. Winker, G. Cesana, J. Dufresne, P. Minnis, C. J. Stubenrauch, and S. Zeng, 2010: The GCM Oriented CALIPSO Cloud Product (CALIPSO-GOCCP). *J. Geophys. Res.*, **115**, D00H16, https://doi.org/10.1029/2009JD012251.

Clement, A. C., R. Burgman, and J. R. Norris, 2009: Observational and model evidence for positive low-level cloud feedback. *Science*, **325**, 460–464, https://doi.org/10.1126/science.1171255.

Delworth, T. L., and Coauthors, 2006: GFDL's CM2 global coupled climate models. Part I: Formulation and simulation characteristics. *J. Climate*, **19**, 643–674, https://doi.org/10.1175/JCLI3629.1.

Du, Y., and S.-P. Xie, 2008: Role of atmospheric adjustments in the tropical Indian Ocean warming during the 20th century in climate models. *Geophys. Res. Lett.*, **35**, L08712, https://doi.org/10.1029/2008GL033631.

Emanuel, K. A., 1988: The maximum intensity of hurricanes. *J. Atmos. Sci.*, **45**, 1143–1155, https://doi.org/10.1175/1520-0469(1988)045⟨1143:TMIOH⟩2.0.CO;2.

Gilford, D. M., 2021: pyPI (v1.3): Tropical cyclone potential intensity calculations in Python. *Geosci. Model Dev.*, **14**, 2351–2369, https://doi.org/10.5194/gmd-14-2351-2021.

Gill, A. E., 1980: Some simple solutions for heat-induced tropical circulation. *Quart. J. Roy. Meteor. Soc.*, **106**, 447–462, https://doi.org/10.1002/qj.49710644905.

Graham, N. E., and T. P. Barnett, 1987: Sea surface temperature, surface wind divergence, and convection over tropical oceans. *Science*, **30**, 657–659, https://doi.org/10.1126/science.238.4827.657.

Gray, W. M., 1968: Global view of the origin of tropical disturbances and storms. *Mon. Wea. Rev.*, **96**, 669–700, https://doi.org/10.1175/1520-0493(1968)096⟨0669:Gvotoo⟩2.0.Co;2.

Harada, Y., and Coauthors, 2016: The JRA-55 reanalysis: Representation of atmospheric circulation and climate variability. *J. Meteor. Soc. Japan*, **94**, 269–302, https://doi.org/10.2151/jmsj.2016-015.

Hartmann, D. L., M. E. Ockert-Bell, and M. L. Michelsen, 1992: The effect of cloud type on Earth's energy balance: Global analysis. *J. Climate*, **5**, 1281–1304, https://doi.org/10.1175/1520-0442(1992)005⟨1281:TEOCTO⟩2.0.CO;2.

Joh, Y., and E. Di Lorenzo, 2019: Interactions between Kuroshio extension and central tropical Pacific lead to preferred decadal-timescale oscillations in Pacific climate. *Sci. Rep.*, **9**, 13558, https://doi.org/10.1038/s41598-019-49927-y.

Kawai, H., and T. Koshiro, 2020: Does radiative cooling of stratocumulus strengthen summertime subtropical highs? *CAS/JSC WGNE Research Activities in Earth System Modelling/WMO*, **50**, 11–12.

Kim, H., S. M. Kang, J. E. Kay, and S.-P. Xie, 2022: Subtropical clouds key to Southern Ocean teleconnections to the tropical Pacific. *Proc. Natl. Acad. Sci. (USA)*, **119**, e2200514119, https://doi.org/10.1073/pnas.2200514119.

Klein, S. A., and D. L. Hartmann, 1993: The seasonal cycle of low stratiform clouds. *J. Climate*, **6**, 1587–1606, https://doi.org/10.1175/1520-0442(1993)006⟨1587:TSCOLS⟩2.0.CO;2.

Kobayashi, S., and Coauthors, 2015: The JRA-55 reanalysis: General specifications and basic characteristics. *J. Meteor. Soc. Japan*, **93**, 5–48, https://doi.org/10.2151/jmsj.2015-001.

Kraucunas, I., and D. L. Hartmann, 2007: Tropical stationary waves in a nonlinear shallow-water model with realistic basic states. *J. Atmos. Sci.*, **64**, 2540–2557, https://doi.org/10.1175/JAS3920.1.

Latham, J., and Coauthors, 2008: Global temperature stabilization via controlled albedo enhancement of low-level maritime clouds. *Philos. Trans. Roy. Soc. London A*, **366**, 3969–3987, https://doi.org/10.1098/rsta.2008.0137.

Lindzen, R. S., and S. Nigam, 1987: On the role of sea surface temperature gradients in forcing low-level winds and convergence in the tropics. *J. Atmos. Sci.*, **44**, 2418–2436, https://doi.org/10.1175/1520-0469(1987)044⟨2418:OTROSS⟩2.0.CO;2.

Loeb, N. G., G. C. Johnson, T. J. Thorsen, J. M. Lyman, F. G. Rose, and S. Kato, 2021: Satellite and ocean data reveal marked increase on Earth's heating rate. *Geophys. Res. Lett.*, **48**, e2021GL093047, https://doi.org/10.1029/2021GL093047.

Loeb, N. G., M. Mayer, S. Kato, T. J. Fasullo, H. Zuo, and R. Senan, 2022: Evaluating twenty-year trends in Earth's energy flows from observations and reanalyses. *J. Geophys. Res.*, **127**, e2022JD036686, https://doi.org/10.1029/2022JD036686.

Masunaga, R., H. Nakamura, T. Miyasaka, K. Nishii, and Y. Tanimoto, 2015: Separation of climatological imprints of the Kuroshio Extension and Oyashio fronts on the wintertime atmospheric boundary layer: Their sensitivity to SST resolution prescribed for atmospheric reanalysis. *J. Climate*, **28**, 1764–1787, https://doi.org/10.1175/JCLI-D-14-00314.1.

Masunaga, R., H. Nakamura, B. Taguchi, and T. Miyasaka, 2020: Processes shaping the frontal-scale time-mean surface wind convergence patterns around the Gulf Stream and Agulhas Return Current in winter. *J. Climate*, **33**, 9083–9101, https://doi.org/10.1175/JCLI-D-19-0948.1.

Matsuno, T., 1966: Quasi-geostrophic motions in the equatorial area. *J. Meteor. Soc. Japan*, **44**, 25–43, https://doi.org/10.2151/jmsj1965.44.1_25.

Middlemas, E., A. Clement, and B. Medeiros, 2019: Contributions of atmospheric and oceanic feedbacks to subtropical northeastern sea surface temperature variability. *Climate Dyn.*, **53**, 6877–6890, https://doi.org/10.1007/s00382-019-04964-1.

Minobe, S., A. Kuwano-Yoshida, K. Nobumasa, S.-P. Xie, and R. J. Small, 2008: Influence of the Gulf Stream on the troposphere. *Nature*, **452**, 206–209, https://doi.org/10.1038/nature06690.

Minobe, S., M. Miyashita, A. Kuwano-Yoshida, H. Tokinaga, and S.-P. Xie, 2010: Atmospheric response to the Gulf Stream: Seasonal variations. *J. Climate*, **23**, 3699–3719, https://doi.org/10.1175/2010JCLI3359.1.

Miyamoto, A., H. Nakamura, and T. Miyasaka, 2018: Influence of the subtropical high and storm track on low-cloud fraction and its seasonality over the south Indian Ocean. *J. Climate*, **31**, 4017–4039, https://doi.org/10.1175/JCLI-D-17-0229.1.

Miyamoto, A., H. Nakamura, T. Miyasaka, and Y. Kosaka, 2021: Radiative impacts of low-level clouds on the summertime subtropical high in the south Indian Ocean simulated in a coupled general circulation model. *J. Climate*, **34**, 3991–4007, https://doi.org/10.1175/JCLI-D-20-0709.1.

Miyamoto, A., H. Nakamura, T. Miyasaka, and Y. Kosaka, 2022a: Wintertime weakening of low-cloud impacts on the subtropical high in the south Indian Ocean. *J. Climate*, **35**, 323–334, https://doi.org/10.1175/JCLI-D-21-0178.1.

Miyamoto, A., H. Nakamura, T. Miyasaka, Y. Kosaka, B. Taguchi, and K. Nishii, 2022b: Maintenance mechanisms of the wintertime subtropical high over the south Indian Ocean. *J. Climate*, **35**, 2989–3005, https://doi.org/10.1175/JCLI-D-21-0518.1.

Miyasaka, T., and H. Nakamura, 2005: Structure and formation mechanisms of the Northern Hemisphere summertime subtropical highs. *J. Climate*, **18**, 5046–5065, https://doi.org/10.1175/JCLI3599.1.

Miyasaka, T., and H. Nakamura, 2010: Structure and mechanisms of the Southern Hemisphere summertime subtropical anticyclones. *J. Climate*, **23**, 2115–2130, https://doi.org/10.1175/2009JCLI3008.1.

Morioka, Y., T. Tozuka, and T. Yamagata, 2010: Climate variability in the southern Indian Ocean as revealed by self-organizing maps. *Climate Dyn.*, **35**, 1059–1072, https://doi.org/10.1007/s00382-010-0843-x.

Myers, T. A., C. R. Mechoso, and M. J. DeFlorio, 2018: Coupling between marine boundary layer clouds and summer-to-summer sea surface temperature variability over the North Atlantic and Pacific. *Climate Dyn.*, **50**, 955–969, https://doi.org/10.1007/s00382-017-3651-8.

Myers, T. A., R. C. Scott, M. D. Zelinka, S. A. Klein, J. R. Norris, and P. M. Caldwell, 2021: Observational constraints on low cloud feedback reduce uncertainty of climate sensitivity. *Nat. Climate Change*, **11**, 501–507, https://doi.org/10.1038/s41558-021-01039-0.

Nakamura, H., T. Miyasaka, Y. Kosaka, K. Takaya, and M. Honda, 2010: Northern Hemisphere extratropical tropospheric planetary waves and their low-frequency variability: Their vertical structure and interaction with transient eddies and surface thermal contrasts. *Climate Dynamics: Why Does Climate Vary?*, D. Sun, and F. Bryan, Eds., *Geophys. Monogr.*, Vol. 189, Amer. Geophys. Union, 149–179, https://doi.org/10.1029/2008GM000789.

NASA/LARC/SD/ASDC, 2019: CERES Energy Balanced and Filled (EBAF) TOA and surface monthly means data in netCDF edition 4.1. NASA Langley Atmospheric Science Data Center DAAC, https://doi.org/10.5067/TERRA-AQUA/CERES/EBAF_L3B.004.1.

Niiler, P. P., and E. B. Kraus, 1977: One-dimensional models of the upper ocean. *Modelling and prediction of the upper layers of the ocean*, E. B. Kraus, Ed., Pergamon Press, 143–172.

Norris, J. R., and C. B. Leovy, 1994: Interannual variability in stratiform cloudiness and sea surface temperature. *J. Climate*, **7**, 1915–1925, https://doi.org/10.1175/1520-0442(1994)007⟨1915:IVISCA⟩2.0.CO;2.

Qu, X., A. Hall, S. A. Klein, and P. M. Caldwell, 2014: On the spread of changes in marine low cloud cover in climate model simulations of the 21st century. *Climate Dyn.*, **42**, 2603–2626, https://doi.org/10.1007/s00382-013-1945-z.

Reynolds, R. W., N. A. Rayner, T. M. Smith, D. C. Stokes, and W. Wang, 2002: An improved in situ and satellite SST analysis for climate. *J. Climate*, **15**, 1609–1625, https://doi.org/10.1175/1520-0442(2002)015⟨1609:AIISAS⟩2.0.CO;2.

Rodwell, M. J., and B. J. Hoskins, 2001: Subtropical anticyclones and summer monsoons. *J. Climate*, **14**, 3192–3211, https://doi.org/10.1175/1520-0442(2001)014⟨3192:SAASM⟩2.0.CO;2.

Schneider, T., C. M. Kaul, and K. G. Pressel, 2019: Possible climate transitions from breakup of stratocumulus decks under greenhouse warming. *Nat. Geosci.*, **12**, 163–167, https://doi.org/10.1038/s41561-019-0310-1.

Seager, R., R. Murtugudde, N. Naik, A. Clement, N. Gordon, and J. Miller, 2003: Air-sea interaction and the seasonal cycle of the subtropical anticyclones. *J. Climate*, **16**, 1948–1966, https://doi.org/10.1175/1520-0442(2003)016⟨1948:AIATSC⟩2.0.CO;2.

Seo, H., and Coauthors, 2023: Ocean mesoscale and frontal-scale ocean–atmosphere interactions and influence on large-scale climate: A review. *J. Climate*, **36**, 1981–2013, https://doi.org/10.1175/JCLI-D-21-0982.1.

Stevens, B., S. Bony, and M. J. Webb, 2012: Clouds On-Off Klimate Intercomparison Experiment (COOKIE). [Available online at http://hdl.handle.net/11858/00-001M-0000-0024-580A-3], 12 pp.

Taguchi, B., H. Nakamura, M. Nonaka, and S.-P. Xie, 2009: Influences of the Kuroshio/Oyashio Extensions on air-sea heat exchanges and storm track activity as revealed in regional atmospheric model simulations for the 2003/4 cold season. *J. Climate*, **22**, 6536–6560, https://doi.org/10.1175/2009JCLI2910.1.

Takaya, K., and H. Nakamura, 2001: A formulation of a phase-independent wave-activity flux for stationary and migratory quasigeostrophic eddies on a zonally varying basic flow. *J. Atmos. Sci.*, **58**, 608–627, https://doi.org/10.1175/1520-0469(2001)058⟨0608:AFOAPI⟩2.0.CO;2.

Tang, B., and K. Emanuel, 2012: A ventilation index for tropical cyclones. *BAMS*, **93**, 1901–1912, https://doi.org/10.1175/BAMS-D-11-00165.1.

Tokinaga, H., Y. Tanimoto, S.-P. Xie, T. Sampe, H. Tomita, and H. Ichikawa, 2009: Ocean frontal effects on the vertical development of clouds over the western North Pacific: In situ and satellite observations. *J. Climate*, **22**, 4241–4260, https://doi.org/10.1175/2009JCLI2763.1.

Voigt, A., N. Albern, P. Ceppi, K. Grise, Y. Li, and B. Medeiros, 2021: Clouds, radiation, and atmospheric circulation in the present-day climate and under climate change. *WIREs Clim. Change*, **12**, e694, https://doi.org/10.1002/wcc.694.

Wittenberg, A. T., A. Rosati, N.-C. Lau, and J. J. Ploshay, 2006: GFDL's CM2 global coupled climate models. Part III: Tropical Pacific climate and ENSO. *J. Climate*, **19**, 698–721, https://doi.org/10.1175/JCLI3631.1.

Wood, R., and C. S. Bretherton, 2006: On the relationship between stratiform low cloud cover and lower-tropospheric stability. *J. Climate*, **19**, 6425–6432, https://doi.org/10.1175/JCLI3988.1.

Xie, S.-P., 2023: Subtropical climate: Trade winds and low clouds. *Coupled Atmosphere-Ocean Dynamics: from El Nino to Climate Change*, Elsevier Science.

Xie, S.-P., and S. G. H. Philander, 1994: A coupled ocean-atmosphere model of relevance to the ITCZ in the eastern pacific. *Tellus*, **46A**, 340–350, https://doi.org/10.3402/tellusa.v46i4.15484.

Xie, S.-P., and Coauthors, 2007: A regional ocean-atmosphere model for eastern Pacific climate: Toward reducing tropical biases. *J. Climate*, **20**, 1504–1522, https://doi.org/10.1175/JCLI4080.1.

Yang, L., S.-P. Xie, S. S. P. Shen, J.-W. Liu, and Y.-T. Hwang, 2023: Low cloud-SST feedback over the subtropical Northeast Pacific and the remote effect on ENSO variability. *J. Climate*, **36**, 441–452, https://doi.org/10.1175/JCLI-D-21-0902.1.

Zelinka, M. D., T. A. Myers, D. T. McCoy, S. Po-Chedley, P. M. Caldwell, and P. Ceppi, 2020: Causes of higher climate sensitivity in CMIP6 models. *Geophys. Res. Lett.*, **47**, e2019GL085782, https://doi.org/10.1002/2015GL067416.

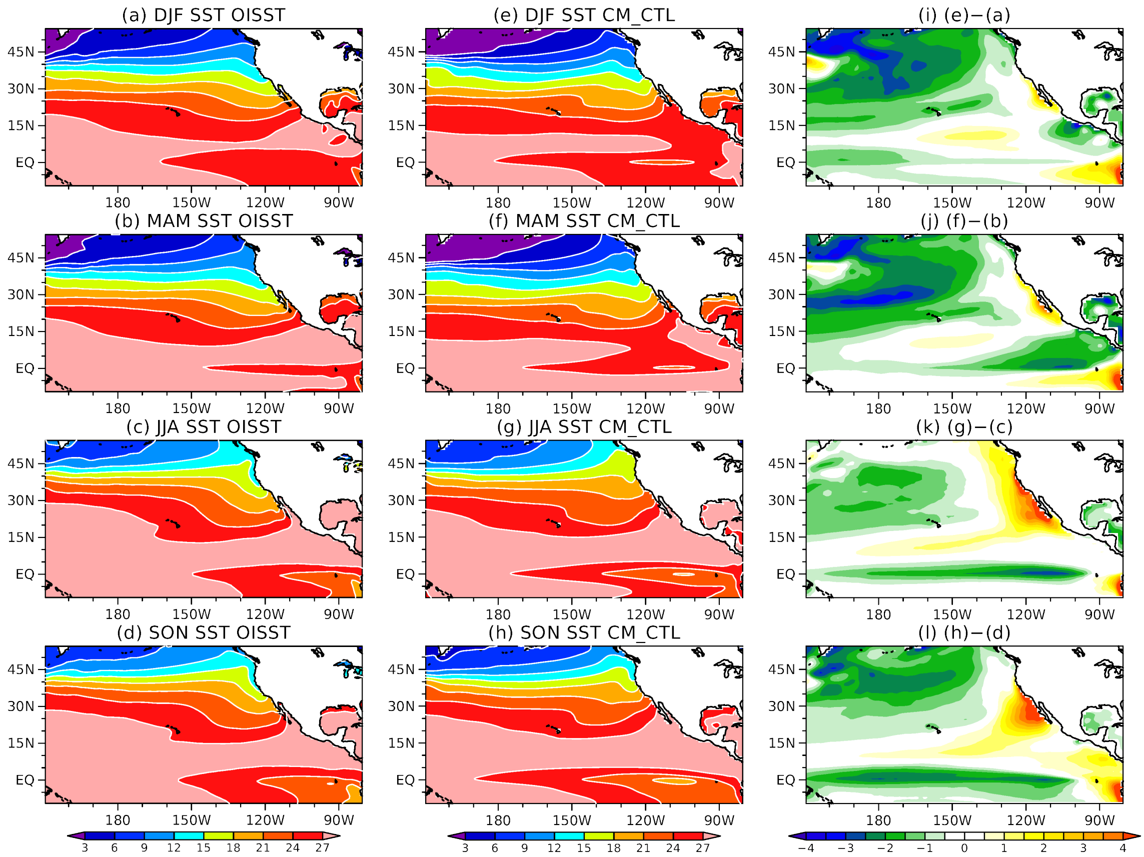

Fig. S1: (a)-(d) Climatological distribution of SST (ºC) in OISST. The coloring convention is indicated at the bottom of (d). (e)-(h) Same as in (a)-(d), respectively, but for CM_CTL. (i)-(l) Same as in (a)-(d), respectively, but for the model bias defined as CM_CTL−OISST.

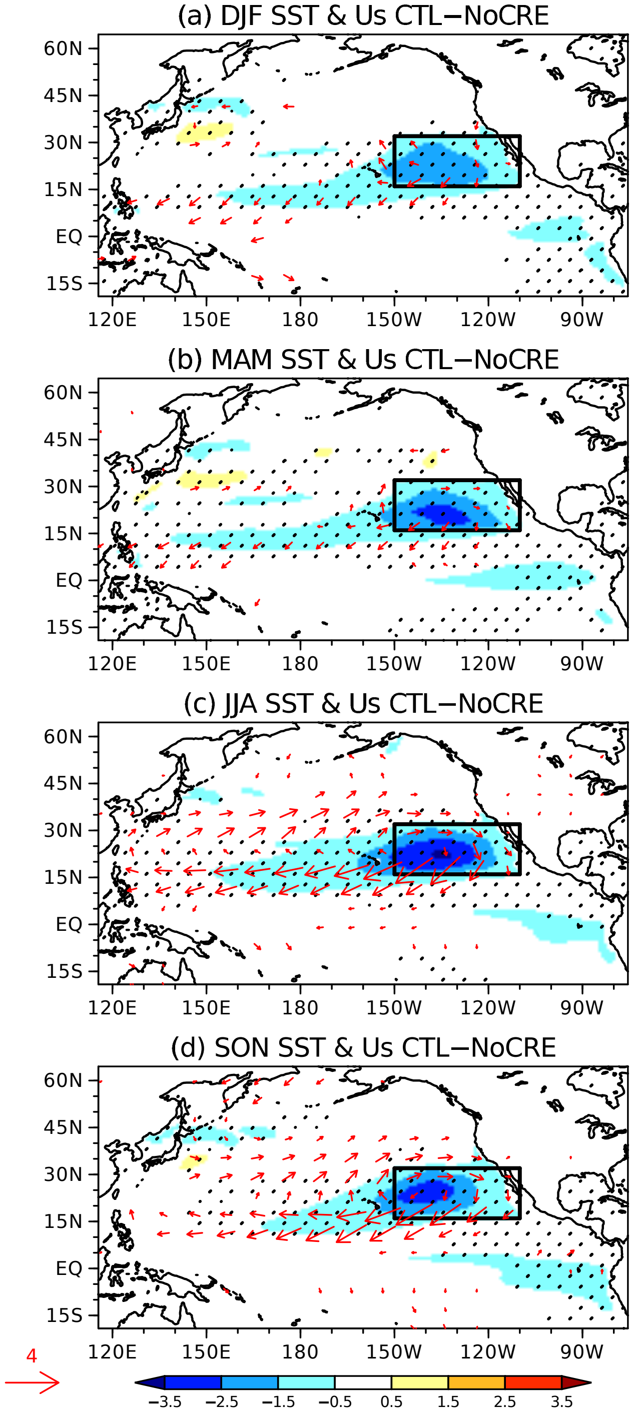

Fig. S2: Response to CRE in the NEP box, represented as the difference defined as CM_CTL−CM_NoCRE. SST (ºC; color shaded as indicated at the bottom) and surface winds (m s^{-1}; red arrows with reference on the left) in (a) DJF, (b) MAM, (c) JJA, and (d) SON. Stippling indicates the 99% confidence for the SST difference. Black box denotes the NEP box, where low clouds are made transparent in CM_NoCRE.

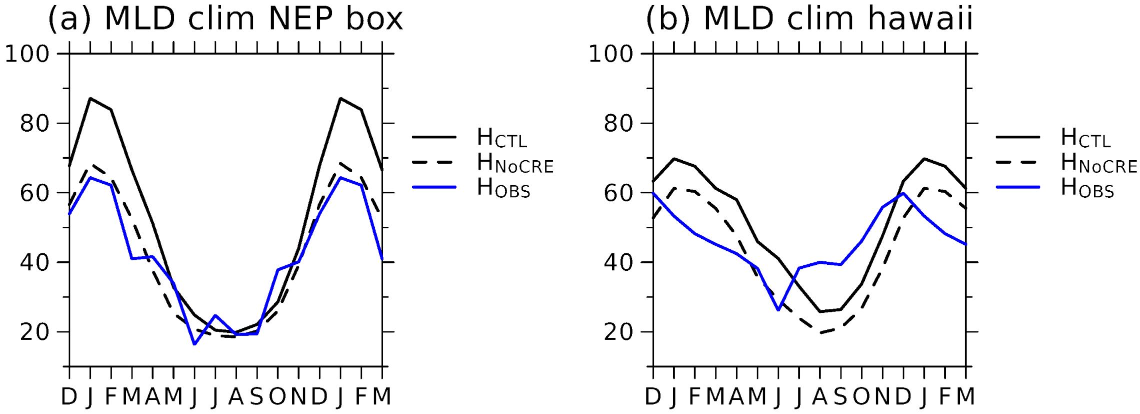

Fig. S3: As in Fig. 6b and 7b, respectively, but with observed MLD (m; blue line) based on the Mixed Layer Dataset of Argo, Grid Point Value (MILA-GPV; Hosoda et al. 2010) for the 2001–18 period. The horizontal resolution of MILA-GPV is 1º in both longitude and latitude. The MLD is defined as a depth at which potential density difference is 0.03 kg m^{-3} relative to the surface. This difference corresponds to buoyancy difference of 0.00029 m s^{-2} with typical seawater density (1026 kg m^{-3}) and the acceleration of gravity (9.8 m s^{-2}), which is close to the definition of MLD employed in our AOGCM (buoyancy difference of 0.0003 m s^{-2}).

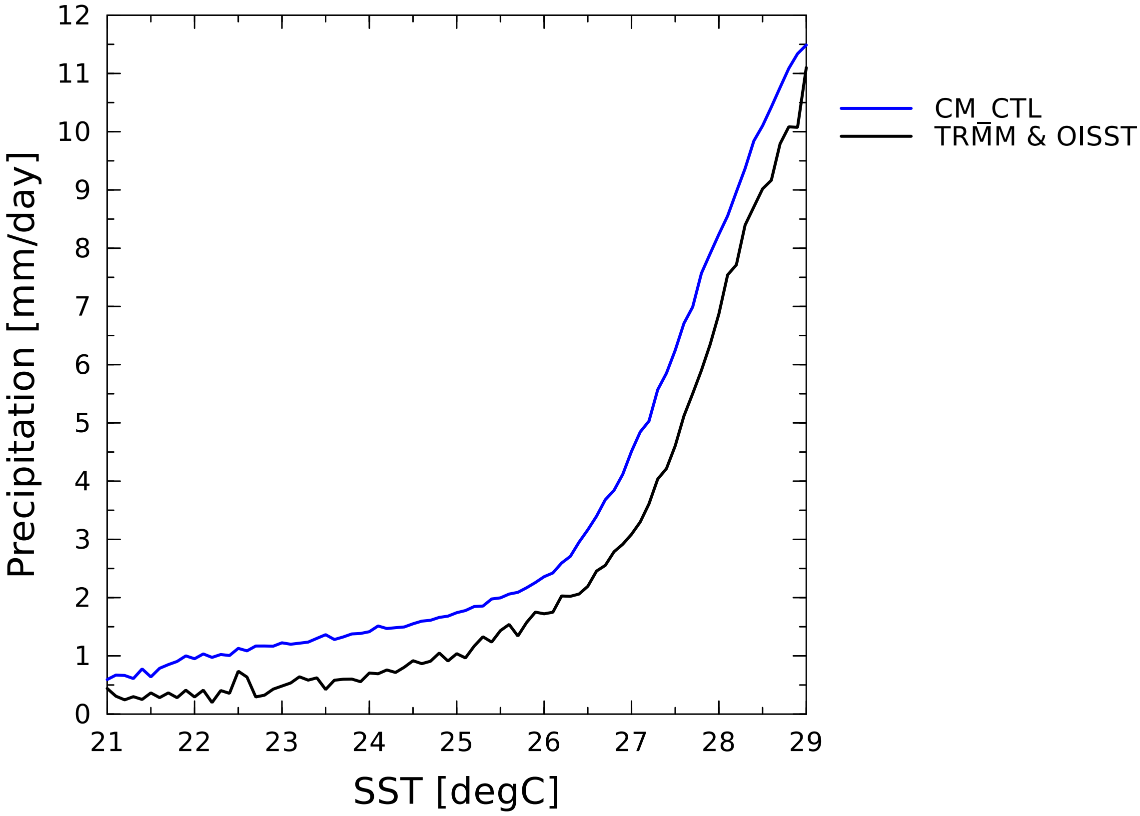

Fig. S4: Dependence of grid-mean monthly precipitation (mm day^{-1}, ordinate) on underlying SST (0.1ºC bin interval, abscissa) in the northeastern Pacific (5ºN-20ºN, 180º-110ºW). Blue and black lines indicate the dependence derived from CM_CTL and observations based on monthly-mean Tropical Rainfall Measuring Mission (TRMM) 3B42 precipitation (Huffman et al. 2007) and OISST in the 1998-2014 period, respectively. Here, all the data are regridded onto a 2.5º grid.

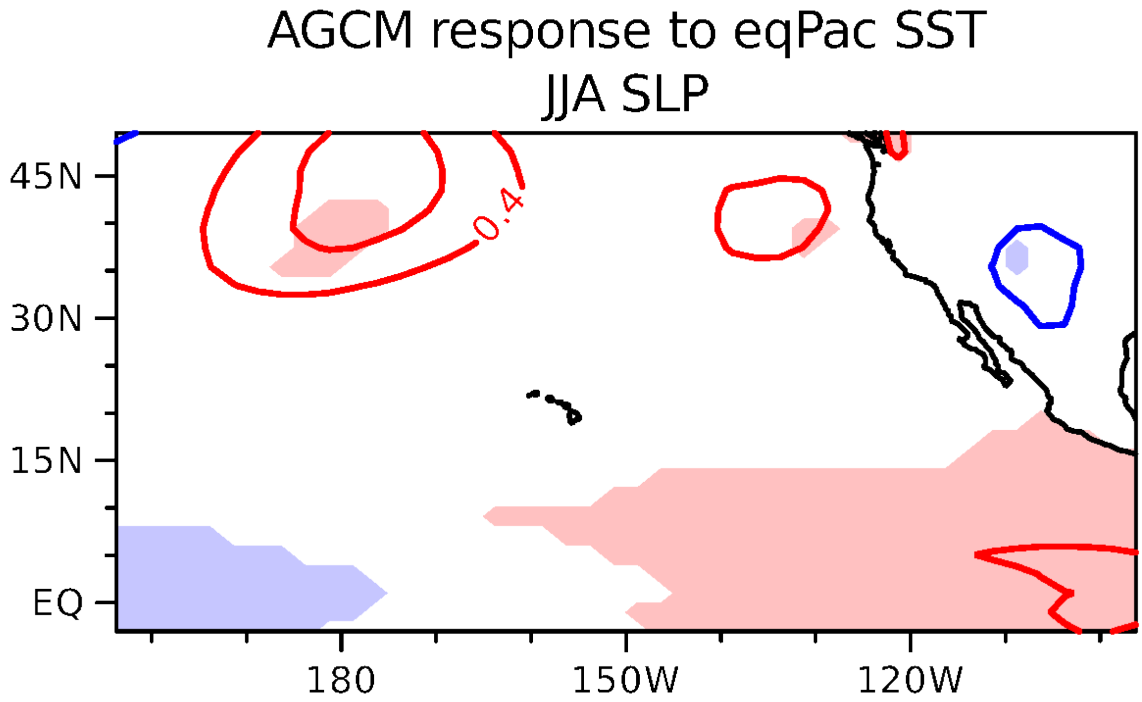

Fig. S5: As in Fig. 9a, but for SST effect in the equatorial Pacific. Like Fig. 9a (AM_CTL−AM_NEPsst), this figure is based on AM_CTL and an AM2.1 experiment, in which SST anomalies are prescribed only in the equatorial Pacific (10ºS-10ºN).

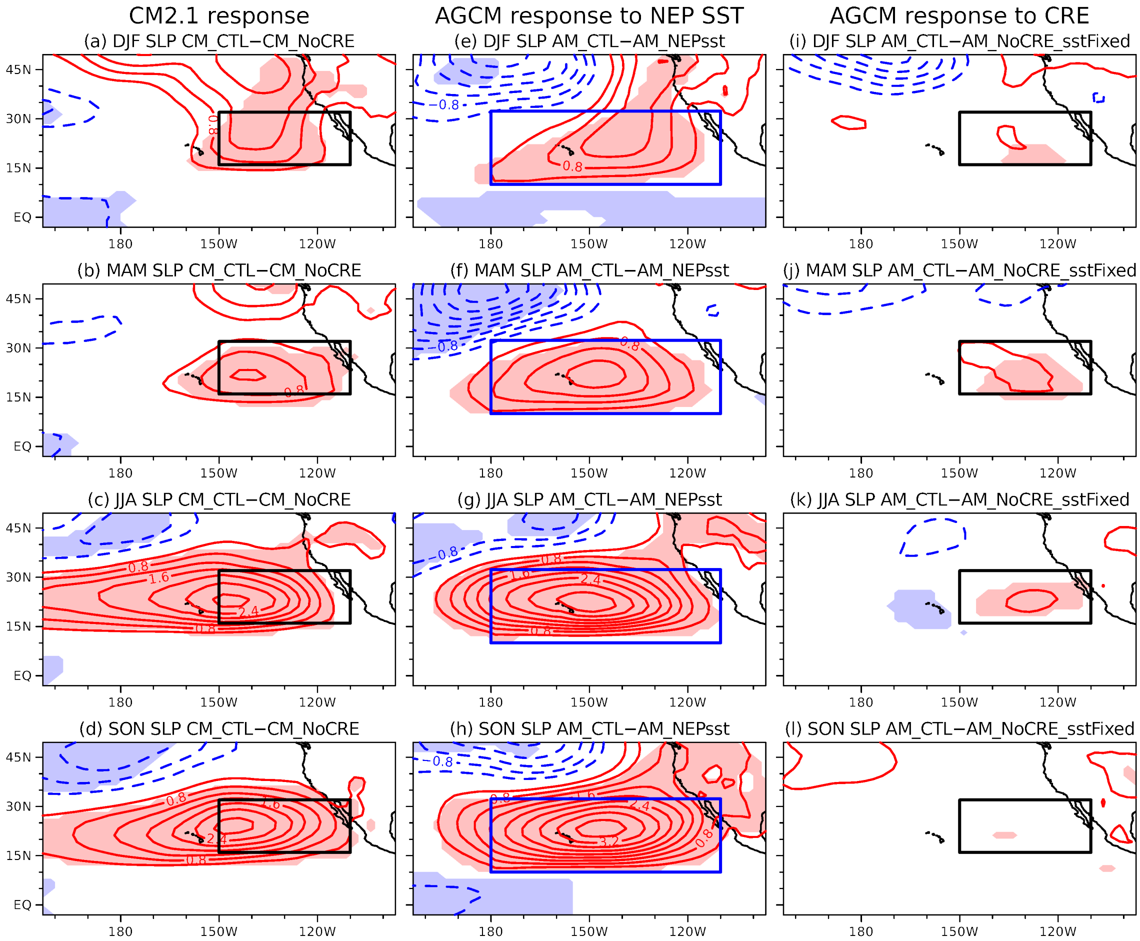

Fig. S6: (a)-(d) SLP response (hPa; color shaded as indicated at the bottom) to CRE in the NEP box, represented by the difference defined as CM_CTL−CM_NoCRE, in (a) DJF, (b) MAM, (c) JJA, and (d) SON. (e)-(h) As in (a)-(d), respectively, but for atmospheric response to anomalous SST over the NEP (AM_CTL−AM_NEPsst). (i)-(l) As in (a)-(d), but for atmospheric response to CRE without SST change (AM_CTL−AM_NoCRE_sstFixed). Color shading indicates the 99% confidence for the difference. Black box in (a)-(d) and (i)-(l) denotes the NEP box, where low clouds are made transparent in CM_NoCRE and AM_NoCRE_sstFixed, whereas blue box in (e)-(h) denotes the domain where SST anomalies are prescribed in AM_NEPsst.

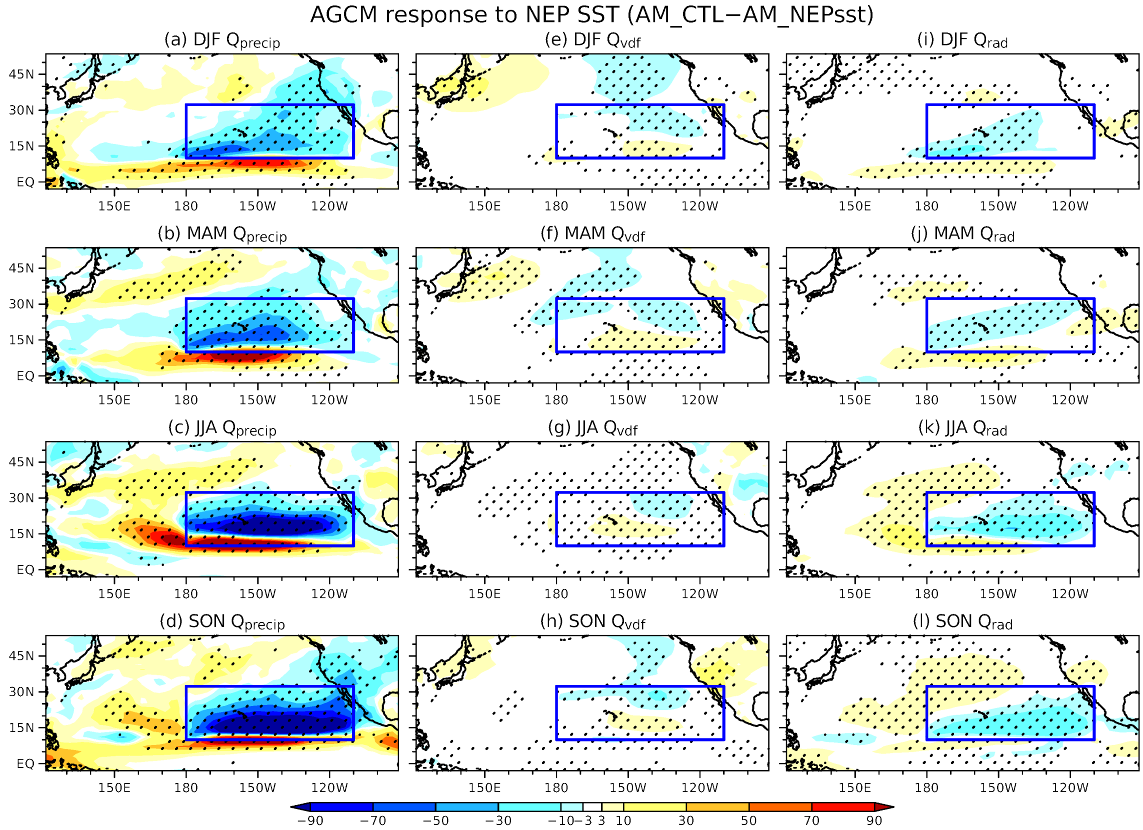

Fig. S7: Atmospheric response to anomalous SST over the NEP, represented by the difference defined as AM_CTL−AM_NEPsst. Vertically integrated Q_{precip} (W m^{-2}; color shaded as indicated at the bottom) in (a) DJF, (b) MAM, (c) JJA, and (d) SON. (e)-(h) As in (a)-(d), respectively, but for Q_{vdf}. (i)-(l) As in (a)-(d), respectively, but for Q_{rad}. Stippling indicates the 99% confidence for the difference. Blue box denotes the domain where SST anomalies are prescribed in AM_NEPsst.

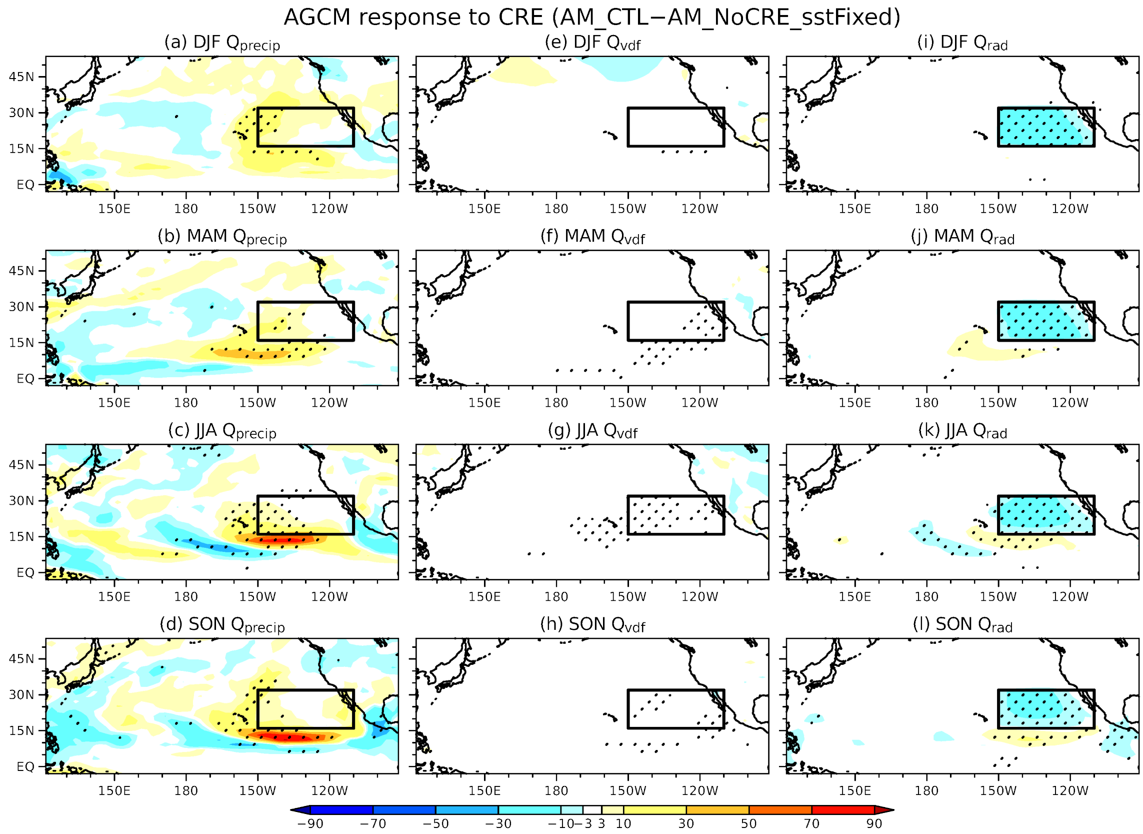

Fig. S8: Atmospheric response to CRE in the NEP box, represented by the difference defined as AM_CTL−AM_NoCRE_sstFixed. Vertically integrated Q_{precip} (W m^{-2}; color shaded as indicated at the bottom) in (a) DJF, (b) MAM, (c) JJA, and (d) SON. (e)-(h) As in (a)-(d), respectively, but for Q_{vdf}. (i)-(l) As in (a)-(d), respectively, but for Q_{rad}. Stippling indicates the 99% confidence for the difference. Black box denotes the NEP box, where we made low clouds transparent in AM_NoCRE_sstFixed.

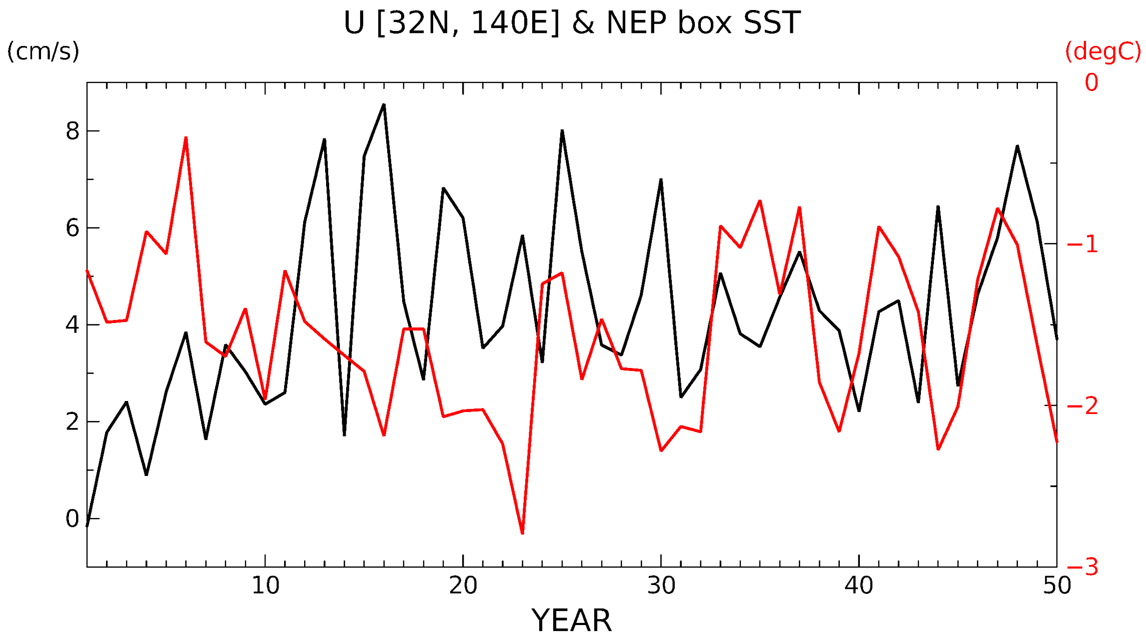

Fig. S9: Time series of annual-mean response to CRE over the NEP box after the simulations are branched off. Eastward surface current along Kuroshio [32ºN, 140ºE] (cm/s; black line) and SST over the NEP box (ºC; red line).

References

Hosoda, S., T. Ohira, K. Sato, and T. Suga, 2010: Improved description of global mixed-layer depth using Argo profiling floats. *J. Oceanography*. **66**, 773-787, https://doi.org/10.1007/s10872-010-0063-3.

Huffman, G. J., and Coauthors, 2007: The TRMM Multisatellite Precipitation Analysis (TMPA): Quasi-global, multiyear, combined-sensor precipitation estimates at fine scales. *J. Hydrometeor.*, **8**, 38–55, https://doi.org/10.1175/JHM560.1.